

Article

Numerical Study of Nanoparticle Coagulation in Non-Road Diesel Engine Exhaust Based on the Principle of Split-Stream Rushing

Yuchen Guo ¹, Pei Wu ^{1,*}, He Su ^{1,*}, Jing Xue ¹ , Yongan Zhang ² and Peiyan Huang ¹

¹ College of Mechanical and Electrical Engineering, Inner Mongolia Agricultural University, Hohhot 010018, China; guoyuchen@emails.imau.edu.cn (Y.G.); jingjingtuizi@126.com (J.X.); 352594342@emails.imau.edu.cn (P.H.)

² College of Computer and Information Engineering, Inner Mongolia Agricultural University, Hohhot 010018, China; zhangya@imau.edu.cn

* Correspondence: jdwp@imau.edu.cn (P.W.); suhe@imau.edu.cn (H.S.)

Abstract: Diesel engines employed in non-road machinery are significant contributors to nanoparticulate matters. This paper presents a novel device based on the principle of split-stream rushing to mitigate particulate matter emissions from these engines. By organizing and intensifying the airflow movement of the jet in the rushing region, the probability of collisions between nanoparticles is enhanced. This accelerates the growth and coagulation of nanoparticles, reducing the number density of fine particulate matter. This, in turn, facilitates the capture or sedimentation of particulate matter in the diesel engine exhaust aftertreatment system. The coagulation kernel function tailored for diesel engine exhaust nanoparticles is developed. Then, the particle balance equation is solved to investigate the evolution and coagulation characteristics. Afterwards, three-dimensional numerical simulations are performed to study the flow field characteristics of the split-stream rushing device and the particle evolution within it. The results show that the device achieves a maximum coagulation efficiency of 59.73%, increasing the average particle diameter from 96 nm to 121 nm. The particle number density uniformity index exceeded 0.93 in most flow regions, highlighting the effectiveness of the device in ensuring consistent particle distribution.

Keywords: non-road diesel engines; split-stream rushing; nanoparticles; coagulation; flow field



Academic Editor: Anastassios M. Stamatelos

Received: 21 November 2024

Revised: 22 December 2024

Accepted: 23 December 2024

Published: 26 December 2024

Citation: Guo, Y.; Wu, P.; Su, H.; Xue, J.; Zhang, Y.; Huang, P. Numerical Study of Nanoparticle Coagulation in Non-Road Diesel Engine Exhaust Based on the Principle of Split-Stream Rushing. *Energies* **2025**, *18*, 40. <https://doi.org/10.3390/en18010040>

Copyright: © 2024 by the authors. Licensee MDPI, Basel, Switzerland. This article is an open access article distributed under the terms and conditions of the Creative Commons Attribution (CC BY) license (<https://creativecommons.org/licenses/by/4.0/>).

1. Introduction

Particulate matters emitted by non-road machinery diesel engines is light in mass and small in volume, making it difficult to settle in the air and capable of long-distance dispersion with the atmosphere. Approximately 53–84% of the primary particulate matters emitted by diesel engines fall within the nanoparticle diameter range [1], with aerodynamic diameters smaller than 50 nm. Due to the unique characteristics of ultrafine particles, respiratory and heart diseases associated with PM exposure may be attributed to ultrafine particulate matters [2,3]. Fine particulate matters can absorb sunlight and energy, leading to increased air temperature and potentially causing global climate issues [4,5]. In response to concerns over particulate matter emissions and pollution, countries worldwide have enacted emission regulations specifically for agricultural machinery diesel engines [6–9]. The application of non-road machinery diesel engines differs significantly from those of on-road diesel engines. Non-road diesel engines typically operate under medium to low

speeds, high loads, and in harsh environments characterized by extreme cold and high temperatures, making particulate matters difficult to control and regulate. Consequently, the level of particulate matter emissions control in non-road machinery diesel engines remains relatively low.

The coagulation process is a dominant mechanism in the evolution of particles [10]. There are many coagulation methods for fine particles in current industrial applications, primarily including electrostatic coagulation, acoustic coagulation, magnetic coagulation, and chemical coagulation [11–14]. Each method has a unique mechanism and feature for controlling the coagulation of fine particles. Various particle coagulation methods are shown in Table 1.

Table 1. Particle coagulation methods.

Coagulation Methods	Mechanisms	Features	Applications
Electrostatic Coagulation	Differential charging of fine particles in an electric field leads to collisions and coagulation due to varying electrostatic forces.	The coagulation efficiency is influenced by the particle concentration, size, and charge distribution, as well as the applied electric field strength.	Removal of fine particles from coal-fired power plants.
Acoustic Coagulation	High-intensity sound field enhances the collision frequency of fine particles, promoting their growth and coagulation into larger particles.	The coagulation efficiency is highly sensitive to changes in acoustic frequency and exhibits a linear relationship with sound pressure level.	Most remain at the laboratory research stage.
Magnetic Coagulation	Magnetic fine particles, pre-magnetized by an external field, collide under the influence of magnetic dipole and gradient forces, coagulating into larger particles.	Pre-magnetization enhances particle sieving, but magnetizing weakly magnetic or non-magnetic particles remains challenging.	Metallurgy, electroplating, wastewater treatment
Chemical Coagulation	The formation of larger agglomerates is achieved by the adsorption and aggregation of fine particles with flocculant droplets through flocculation.	The flocculant concentration, along with pH value, flow rate, and type, significantly influences the removal efficiency of fine particles.	Removal of PM2.5 particles from coal-fired power plant.

Impinging jet flow is formed by the collision of two or more opposite jets or free jets against solid walls. The region where the jets collide with each other exhibits significant relative velocity and pressure gradient, which enhances momentum, heat, and mass transfer in relevant reaction processes [15,16]. Impinging jet mixers/reactors (IJM/IJR) is the major application of impinging jet technology in industrial processes. Many efforts have been made to study the flow field characteristics of IJM/IJR with various geometric structures and flow velocities. Zhang et al. [17] investigated the flow field characteristics of a double-layer impinging jet reactor. It was found that the vorticity increased with an increase in flow velocity, and the highest vorticity occurred at the surfaces of the two impinging jets. These high-intensity vortices interacted with each other and transferred energy, which contributed to enhancing the mixing efficiency. Liu et al. [18] conducted PIV experiments and numerical simulations to investigate the influence of various inlet velocity fluctuations on the velocity and turbulence in the impingement region of an impinging jet reactor. The results demonstrated that, compared with traditional impinging jet reactors with constant inlet velocities, impinging jet reactors with fluctuating inlet flow conditions can generate more intense turbulence in the impingement region, which can instantaneously

shift the impingement point. Pal et al. [19] investigated the turbulence and the mixing performance of liquid-impinging jets in a modified geometry impinging jet reactor and found that it reduces wall deposition compared to the conventional design. Lindstedt et al. [20] conducted PIV experiments on a coaxial impinging jet produced by a pair of nozzles, their findings revealed a substantial enhancement in the axial and radial normal stresses towards the impingement surface, with increases of 300% and 160%, respectively. Hao et al.'s study [21] on the airflow mixing effect of a cylindrical confined impinging jet mixer showed that the large-scale circulating flow can feedback disturbances to the main jet, causing large, rapid, and highly random movements at the jet impingement point, and the mixer has the best mixing effect on the airflow when the Reynolds number is 600 and 1000. Zhang et al. [22] performed an experimental study on the flow field characteristics of symmetrical and asymmetrical flow fields in the two-layer impinging stream mixer. It was found that, in the asymmetrical flow field, the flow field energy was higher compared to the symmetrical flow field, but the mixing rate was lower. Bie et al. [23] performed experiments and three-dimensional numerical simulations of a T-T impinging jet reactor and found that the secondary impingement in the T-T jet reactor enhances the mixing performance dramatically, particularly in vortex, and unsteady symmetric flow regimes.

Many studies have also been conducted regarding the characteristics of particles within impinging jets. Yin et al. [24] performed a large eddy simulation (LES) of the formation of pollutant nanoparticles in a vehicular exhaust with an impinging twin jet. The results showed that particle size is maximum near the free jet region, while number concentration decreases markedly following coagulation. Liu et al. [25] investigated the particle movement in two-phase impinging streams. The findings demonstrated the formation of two pairs of counter-rotating gas vortices on either side of the opposing jet flows. These vortices effectively entrained particulate matter, leading to a significant reduction in particle deposition. Hubbard et al. [26] investigated the aerosol formation by using the computational fluid dynamics (CFD) method to study the flow patterns within an impinging jet reactor. It was found that streamlines adjacent to the diffuser plate exhibit recirculation patterns. Li et al. [27] examined the nanoparticle production process in a confined impinging jet mixer and showed that a lower mixing velocity and higher turbulence viscosity existed compared with no aggregation.

The application of nanoparticle coagulation and the impinging jets have been extensively studied in theory, experiments, and simulations. However, most studies have focused on nanoparticle synthesis, precipitation processes, and industrial dust removal, with a lack of studies on the evolution and coagulation characteristics of nanoparticles in diesel engine exhaust. Therefore, in this paper, a novel device based on the principle of split-stream rushing is proposed to reduce the number of particles. By intensifying the airflow in the rushing region between the two pairs of impinging jet-like flows, the collision probability and coagulation rate of nanoparticles are increased, leading to particle sizes increased and number concentrations reduced. This will facilitate the capture or sedimentation of particles by the diesel engine's aftertreatment system, achieving a further reduction in the number concentration of particulate matter emissions. Firstly, a mathematical model is established to describe the evolution of nanoparticle dynamics based on their kinetic characteristics and physical mechanisms, and a particle coagulation kernel function is constructed that matches the diameter range of diesel engine exhaust nanoparticles. Secondly, the particle population balance equation is coupled with the Reynolds-averaged Navier–Stokes equations in the Eulerian framework to obtain the evolution and distribution of fine particles in the split-stream rushing device under the influence of airflow. The flow field characteristics at key locations within the split-stream rushing device and their effects on the evolution of particle number density (PND) and coagulation efficiency are investigated.

2. Materials and Methods

The mathematical model currently used to describe the dynamic evolution of particles is based on their kinetic characteristics and corresponding physical mechanisms. The Eulerian framework focuses on the statistical properties of particle groups without requiring the tracking of individual particle movements. It is more efficient when dealing with large quantities of particles, being the preferred method for describing the discrete phase in the current paper. The coagulation kernel function is also used to control the coagulation rate of nanoparticles.

2.1. Two-Phase Computational Fluid Dynamics

The particle discrete system consists of both the discrete phase and the continuous phase.

The Reynolds-Averaged Navier–Stokes (RANS) method transforms nonlinear partial differential equations into integral-differential equations for solving these nonlinear equations. Due to its relatively lower computational requirements, RANS is more commonly used in engineering applications and research. The RNG k-epsilon models were implemented in numerical simulations in the current paper to model the unknown terms in the Reynolds stress tensor within the RANS framework. They consist of two transport equations for the turbulent kinetic energy k and the dissipation rate ε can be expressed as follows:

$$\frac{\partial(\rho k)}{\partial t} + \frac{\partial(\rho k u_i)}{\partial i} = \frac{\partial}{\partial j} \left[\left(\mu + \frac{\mu_t}{\sigma_k} \right) \frac{\partial k}{\partial j} \right] + \frac{\partial u_j}{\partial i} \left(2\mu_t S_{ij} - \frac{2\mu_t}{3} \vec{\nabla} \cdot \vec{u} \delta_{ij} \right) - \rho \varepsilon \quad (1)$$

$$\frac{\partial(\rho \varepsilon)}{\partial t} + \frac{\partial(\rho \varepsilon u_i)}{\partial i} = \frac{\partial}{\partial j} \left[\left(\mu + \frac{\mu_t}{\sigma_\varepsilon} \right) \frac{\partial \varepsilon}{\partial j} \right] + C_{\varepsilon 1} \frac{\varepsilon}{k} \frac{\partial u_j}{\partial i} \left(2\mu_t S_{ij} - \frac{2\mu_t}{3} \vec{\nabla} \cdot \vec{u} \delta_{ij} \right) - C_{\varepsilon 2} \rho \frac{\varepsilon^2}{k} \quad (2)$$

where σ_k , σ_ε , $C_{\varepsilon 1}$, $C_{\varepsilon 2}$ are empirical parameters, and where $\sigma_k = 1.0$, $\sigma_\varepsilon = 1.3$, $C_{\varepsilon 1} = 1.44$, $C_{\varepsilon 2} = 1.92$. The turbulent viscosity μ_t is given by Launder and Spalding [28].

$$\mu_t = C_\mu \rho \frac{k^2}{\varepsilon} \quad (3)$$

where $C_\mu = 0.09$.

Nanoparticles in diesel engine exhaust are dispersed within a continuous gas medium. Nanoparticles are generally treated as discrete entities. In numerical simulations of two-phase flow, it is essential to consider not only the conservation of mass, momentum, and energy for the continuous-phase fluid but also the equilibrium relationships of internal variables in discrete-phase particle dynamic events.

The population balance equation (PBE) is a continuous function that describes the evolution of the number density function (NDF) of discrete particles. It governs the evolution process of the number density function, which is assumed to exist within the population of discrete phase elements. When coagulation occurs only between discrete-phase particles, and the internal variables are the volumes v and v' of the discrete phase, the PBE can be expressed as follows:

$$\frac{\partial n(t, x, v)}{\partial t} = \frac{1}{2} \int_0^v \beta(v - v', v') n(v - v', t) n(v', t) dv' - n(v, t) \int_0^\infty \beta(v, v') n(v', t) dv' \quad (4)$$

where $n(t, x, v)$ is the particle diameter distribution function at time t , and position x for particles with volume v . v and v' represent the particle volume. $n(v, t) dv$ denotes the PND within the volume range v to $v + dv$ per unit volume. $\beta(v, v')$ is the collision kernel function for particles of volumes. The first term on the right-hand side of the equation represents the rate of volume increase due to the coagulation of particles with volumes $v - v'$ and v .

The second term on the right-hand side represents the rate of volume decrease due to the coagulation of particles with volume v .

2.2. Sectional Method

Since the PBE is a hyperbolic integro-partial differential transport equation characterized by strongly nonlinear integral source terms and is difficult to obtain an analytical solution, numerical methods are required to solve the PBE.

The sectional method approximates the continuous particle diameter distribution using a finite number of m discrete nodes [29]. By establishing balance equations, the evolution of the particle distribution function over time can be obtained. In the sectional method, when the internal variables are the discrete-phase particle volumes v and v' , the internal variable $\zeta = v$ is divided into m intervals using $m + 1$ grid points (v_1, v_2, \dots, v_{m+1}). The i -th interval is denoted as follows:

$$N_i(t, \mathbf{x}) = \int_{v_{i-1}}^{v_i} n(t, \mathbf{x}, v) dv \quad (5)$$

where v_{i-1} and v_i represent the minimum and maximum particle diameters, respectively.

By integrating source term equations over the discrete interval v_i to v_{i+1} , the time evolution equation for the PND within the interval can be expressed as follows:

$$\frac{dN_i(t, \mathbf{x})}{dt} = \frac{1}{2} \int_{v_i}^{v_{i+1}} dv \int_0^v n(v - v', t) n(v', t) \beta(v - v', v') dv' - \int_{v_i}^{v_{i+1}} n(v, t) dv \int_0^\infty n(v', t) \beta(v, v') dv' \quad (6)$$

2.3. Coagulation Kernel Function for Nanoparticles

In particle population balance simulations, all intrinsic mechanisms influencing the evolution of nanoparticles are encapsulated within the kernels of various events. The physical significance of these kernels is the rate at which these events occur. The coagulation of nanoparticles emitted by diesel engines in a flow field is driven by both Brownian motion and turbulence. To study the coagulation phenomenon caused by particle collisions, this research employs a collision kernel model. This model assumes that particles coagulate immediately after colliding due to Brownian motion.

The expression of the coagulation kernel β varies for different particle diameter ranges. The interaction between air and particles in the free molecular regime is discontinuous. The mass, momentum, and energy exchange between particles and gas in this regime can be determined by the Boltzmann equation. Consequently, the collision kernel function of particles in the free molecular regime can be calculated as follows [30]:

$$\beta_B^{fm}(u, v) = K_{fm} (u^{-1} + v^{-1})^{1/2} (u^{1/3} + v^{1/3})^2 \quad (7)$$

$$K_{fm} = \left(\frac{3}{4\pi} \right)^{1/6} \left(\frac{6k_B T}{\rho_p} \right)^{1/2} \quad (8)$$

where u and v represent the volumes of two particles; K_{fm} is the collision coefficient; and k_B is the Boltzmann constant.

The functions for particle coagulation in the free molecular regime can be extended to the continuum regime. In the continuum regime, the coagulation kernel function for particles is given by the following:

$$\beta_B^{co}(u, v) = K_{co} (u^{-1/3} + v^{-1/3}) (u^{1/3} + v^{1/3}) \quad (9)$$

where K_{co} is the particle diffusion coefficient.

$$K_{co} = 2K_B T / \mu \quad (10)$$

where μ , the dynamic viscosity of air, is given by Sutherland's law [31].

$$\mu = \mu_{23} (T/T_0)^{3/2} \left(\frac{T_0 + T_s}{T + T_s} \right) \quad (11)$$

The coagulation kernel function in the near-continuum regime is typically given by the following:

$$\beta_B^{co/sf}(u, v) = K_{co} \left[\frac{C(u)}{u^{1/3}} + \frac{C(v)}{v^{1/3}} \right] (u^{1/3} + v^{1/3}) \quad (12)$$

where $C(u)$ is the Stokes–Cunningham slip correction factor. For the continuum-slip regime, the slip correction factor has several forms, with a commonly used expression [32,33]:

$$C = 1 + Kn[A_1 + A_2 \exp(-A_3/Kn)] \quad (13)$$

where $A_1 = 1.142$, $A_2 = 0.558$, and $A_3 = 0.999$.

In the transition regime, the particle diameter range encompasses both the free molecular regime and the continuum regime. Therefore, coagulation kernel functions that describe particles in the free molecular or continuum regimes cannot be directly applied to the transition regime. Numerous theories have been widely discussed in the literature to calculate the collision kernel function in the transition regime. Otto et al. [34], and others have proposed an interpolated expression for the collision kernel function in the transition regime, given by the following:

$$\beta_B^{tr} = \frac{\beta_B^{fm} \beta_B^{co}}{\beta_B^{fm} + \beta_B^{co}} \quad (14)$$

On the theories of Otto et al. [35] proposed a more accurate all-regime particle collision kernel function, which is given by the following:

$$\beta_B^{entire}(u, v) = \beta_{co} \cdot f(Kn) \quad (15)$$

The correction factor model is given by the following [36]:

$$f(Kn) = \frac{1 + Kn_d}{1 + 2Kn_d + 2Kn_d^2} \quad (16)$$

where $Kn_d = 1/2(\beta_B^{co}/\beta_B^{fm})$.

Turbulent effects in the flow field induce turbulent fluctuations in the movement of nanoparticles. These turbulent fluctuations also alter the relative motion of the particles, thereby affecting their coagulation process.

Diesel exhaust nanoparticles are zero-inertia particles that fully follow the fluid motion, and the relative motion between particles is influenced by the dissipation of small-scale eddies, meaning that the collision rate is determined solely by the interaction between particles and the energy-dissipating small-scale eddies [37]. In isotropic turbulence, the turbulent coagulation kernel function for zero-inertia particles is given by the following:

$$\beta_T^{zi} = 2\pi R^2 \left(\frac{2}{\pi} \right)^{1/2} \left(\frac{R^2 \varepsilon}{15 \nu} \right)^{1/2} = 1.294 \frac{(r_1 + r_2)^3}{\tau_k} \quad (17)$$

Turbulence and Brownian motion occur on different scales, and these processes can be considered statistically independent [38]. Therefore, the combined effect of turbulent

motion and Brownian motion on particle coagulation can be represented by the following compound coagulation function:

$$\beta^{\text{total}} = \left[\left(\beta_{\text{B}}^{\text{entire}} \right)^2 + \left(\beta_{\text{T}}^{\text{zi}} \right)^2 \right]^{1/2} \quad (18)$$

2.4. Simulation Conditions

The principles of split-stream and rushing are realized through the split-stream rushing device depicted in Figures 1 and 2, showing the three-dimensional model. The operating principle is as follows: diesel engine exhaust enters through the airflow inlet and is automatically distributed after passing through a conical guide surface. The flow is then divided and directed through two pairs of rectangular rushing holes into the inner chamber. These rectangular rushing holes serve a dual purpose: (i) organizing the flow movement; and (ii) converting low-velocity airflow into high-velocity airflow, thereby increasing the kinetic energy of the flow. Since each pair of rectangular rushing holes is radially symmetric, the incoming airflow meets at the center with equal velocity but in opposite direction. The two opposing airflow jets, carrying particles of different diameters, collide when they meet.

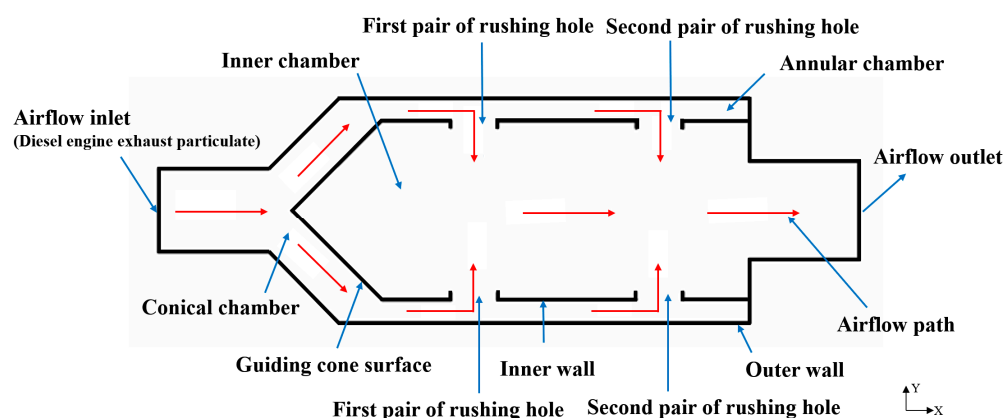


Figure 1. Sketch of split-stream rushing device.

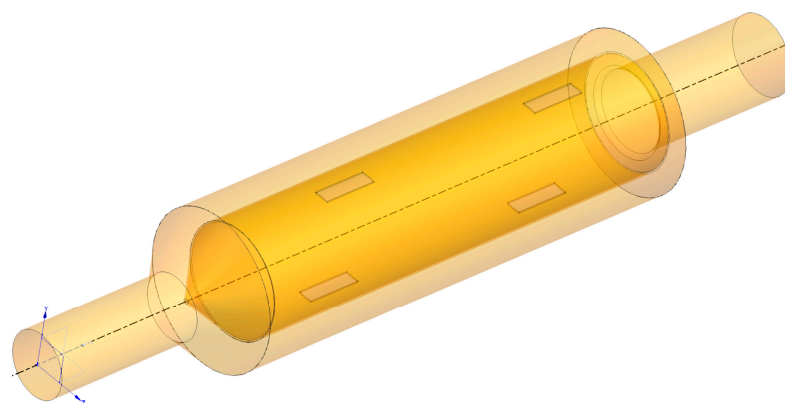


Figure 2. Sketch of three-dimensional model of split-stream rushing device.

The particle population balance equation and flow field equations, which describe the evolution of particle dynamics, are solved using the Ansys Fluent 2019R2 software. Given the low concentration of diesel exhaust particles, the influence of the particle phase on the gas phase is neglected. Eulerian–Eulerian two-phase flow computational model is constructed and solved within a one-way coupling framework.

Under steady-state conditions, experimental and simulation studies [39–41] have shown that the number density of diesel engine exhaust particles typically follows a

unimodal or bimodal log-normal distribution. Since the particle coagulation kernel function constructed in this paper is only applicable to unimodal distributions, the initial particle number density in this study is selected as a unimodal log-normal distribution. The particles are classified into 31-diameter bins (intervals), and the PBE is solved using the homogeneous discretization method.

Figure 3 shows the initial particle number density. The total volume fraction of the particle phase is 1×10^{-6} . The particles are standard carbon particles with a density of 2000 kg/m^3 .

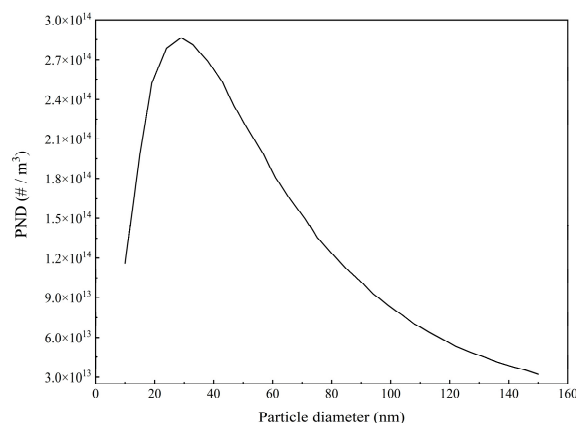


Figure 3. Initial particle number density. (“#” refers to the particle number, the same below).

The inlet boundary employs a velocity inlet model, while the outlet boundary uses a pressure outlet model, and a no-slip boundary condition is applied to the walls. Table 2 presents the inlet boundary conditions corresponding to the operating conditions of the diesel engine. The velocity and temperature presented here were measured from a 1.2 L, 15.7 kW single-cylinder agricultural tractor diesel engine operating at no load in our laboratory. Three engine speeds were tested: low (approximately 1000 rpm), medium (approximately 1500 rpm), and rated (2200 rpm), corresponding to cases 1, 2, and 3, respectively.

Table 2. Inlet boundary conditions.

Parameter	Case 1 (Low Speed)	Case 2 (Medium Speed)	Case 3 (High Speed)
Inflow velocity (m/s)	10	30	50
Inflow temperature (°C)	150	200	250
Inflow viscosity (Pa·s)	2.42×10^{-5}	2.58×10^{-5}	2.76×10^{-5}
Inflow density (kg/m ³)	0.83	0.75	0.68

The particle compound coagulation kernel function was implemented in a user-defined functions (UDF) program in Ansys Fluent and compiled in Visual Studio 2022. The boundary and initial conditions corresponding to the relevant cases were set. The computational time step was set to 0.005 s, with 40 iterations per time step, to solve the particle evolution process from the time steps 0 to 10 s.

The computational mesh for the split-stream rushing device was generated using the HyperMesh 14.0 software. Due to the presence of irregular geometries within the device, only unstructured tetrahedral meshes were created. The maximum surface mesh size is 0.006 m, and the minimum surface mesh size is 0.001 m. The maximum volume mesh size is 0.01 m, and the minimum volume mesh size is 0.0015 m. Local mesh refinement was applied in the airflow jet-rushing region. A total of five layers of wall boundary layers were set, with the first wall boundary layer thickness set to 2.5×10^{-4} m to ensure the Y+

value close to 30. The boundary layer growth rate was set to 1.1, and the minimum mesh orthogonality ratio was 0.26.

The mesh independence study was conducted to ensure that the results of the CFD simulations were independent of the mesh resolution. Five different mesh sizes were generated for this purpose. The simulation results show that when the mesh size reaches or exceeds 2,366,306 cells, the outlet PND and outlet velocity no longer change significantly with increasing cell numbers. Consequently, a mesh with 2,366,306 cells was chosen for the subsequent simulations.

3. Results and Discussion

3.1. Model Validation

To validate the RANS approach, the high-resolution large eddy simulation (LES) results are employed as a reference to evaluate the accuracy of RANS simulations in predicting key flow features, including velocity, pressure, and turbulent kinetic energy in the impingement region. Figure 4 presents the velocity and turbulent kinetic energy (TKE) along the X-axis obtained from both LES and RANS simulations for the case of a 30 m/s inlet velocity. While the mean velocities from both models exhibit relatively small differences at the inlet pipe, rushing holes, and outlet pipe, the RANS results consistently underestimate the mean velocity compared to LES, with a minimum difference of 77% at $x = 0.358$ m. These discrepancies can be attributed to the fundamental differences between the two methods in resolving turbulence, capturing flow field details, and representing turbulent energy distribution. LES directly resolves most of the turbulent structures, leading to a more accurate representation of energy distribution in the flow field and potentially higher local velocities in certain regions. In contrast, RANS models treat turbulence as part of the mean flow field and employ concepts such as turbulent viscosity. This approach is more inclined to capture the mean flow behavior rather than instantaneous fluctuations, which may result in under-prediction of velocities in regions with strong turbulence.

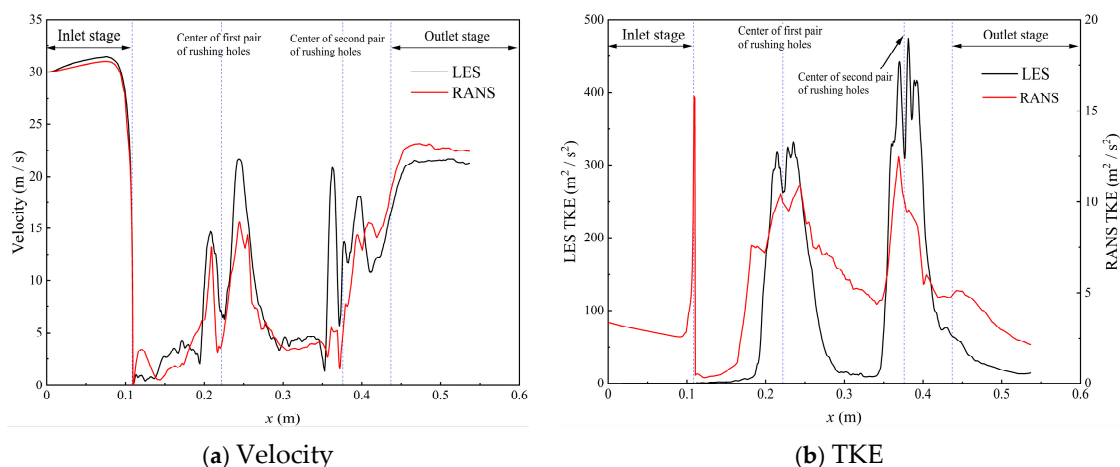


Figure 4. Velocity and TKE along the X-axis obtained from both LES and RANS of case 2.

Figure 4 also presents the TKE distributions obtained from LES and RANS simulations for the case of 30 m/s inlet velocity. A significant discrepancy is observed between the two models. The LES results show much higher TKE levels compared to RANS, primarily due to the direct resolution of large-scale eddies in LES, which captures a substantial portion of the turbulent kinetic energy. RANS models, on the other hand, rely on turbulence models to represent turbulent effects, providing estimates of TKE and dissipation rate based on overall, averaged flow field characteristics. In complex flow regions such as the rushing zone, where significant energy transfer and high velocity gradients occur, RANS models

may fail to accurately capture local flow details and the contributions of small-scale eddies, especially regarding instantaneous turbulent dissipation. This leads to under-prediction of TKE and different TKE distributions compared to LES. Nevertheless, this discrepancy does not undermine the overall qualitative agreement between the two simulation methods regarding the dominant flow features.

3.2. Particle Coagulation at Flow Splitting Stage

Within the axial range of 0.11 m to 0.145 m, the airflow is split as it flows over the guiding cone surface and then enters the annular chamber. During this process, the coagulation and distribution of particles change with the characteristics of airflow. Upon reaching the transition position where the guiding cone surface intersects with the annular chamber, the airflow impinges upon the wall and subsequently separates. The results show that there is a distinct annular vortex ring in the airflow passing through the guiding cone surface, as shown in Figure 5.

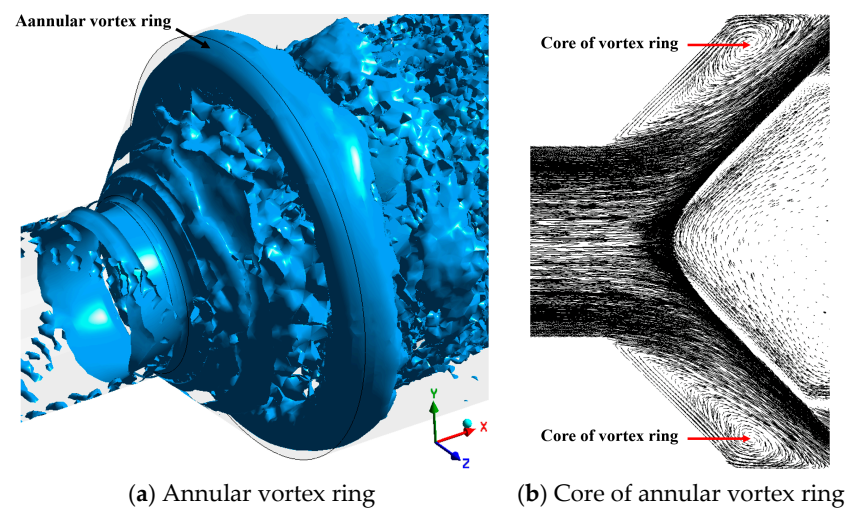


Figure 5. Sketch of annular vortex ring in conical chamber.

In order to study the influence of the flow field structure on the coagulation of nanoparticles in the complex annular vortex ring and its surrounding flows, several key locations are identified. Four circles, denoted as circle A, circle B, circle C, and circle D shown in Figure 6, are selected around the central X-axis to investigate the effect of the vortex within the conical chamber on particle coagulation.

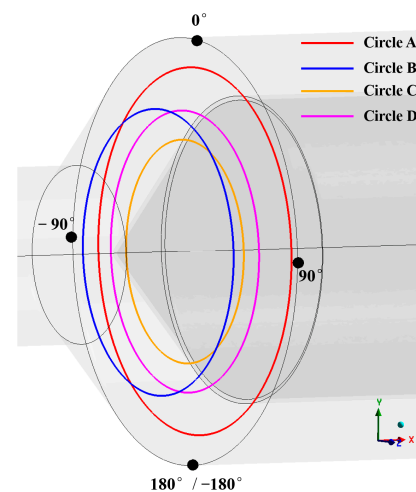


Figure 6. Key airflow locations in conical chamber.

Circle A is located at the center of the vortex, where the vortex flow reaches a relatively stable state. The size and shape of the vortex are relatively fixed, and the magnitude and direction of the airflow exhibit a certain degree of regularity and predictability. Circle B is located at the outer periphery of the vortex. Circle C is located in the main flow region, while circle D is located at the transition position between the vortex and the main flow, which is the vortex generation region. In this region, the velocity gradient is not only large in the main flow direction but also large in the direction perpendicular to the flow direction. This velocity gradient perpendicular to the flow direction is an important factor in the formation of vortices.

Figure 7 shows the PND distribution on circles A, B, C, and D for three cases. For all cases, the PND at the vortex center on circle A is lower than that in the outer region of the vortex and the main flow region. This is because the pressure is lower in the vortex core zone, and the surrounding airflow entraining particles is drawn into the vortex, increasing the collision frequency of particles and promoting particle coagulation. The PND on circle D is mainly affected by the airflow on circles C and D, and the PND is between that of circles C and B. The PND on circle C is the highest because the velocity on circle C is the highest, which leads to a decrease in the contact time between particles, a reduction in the probability of particle collisions, and a decrease in the number of particles participating in coalescence. The average pressure gradient between circles B, C, and D and circle A is shown in Table 3. The high-pressure gradient is accompanied by an increase in gas flow, indicating that the airflow tends to move towards circle A, which makes it easier for nanoparticles in the airflow to be transported to specific regions by convection. The enhancement of convection can affect the interactions between particles and promote the collision and coagulation of particles.

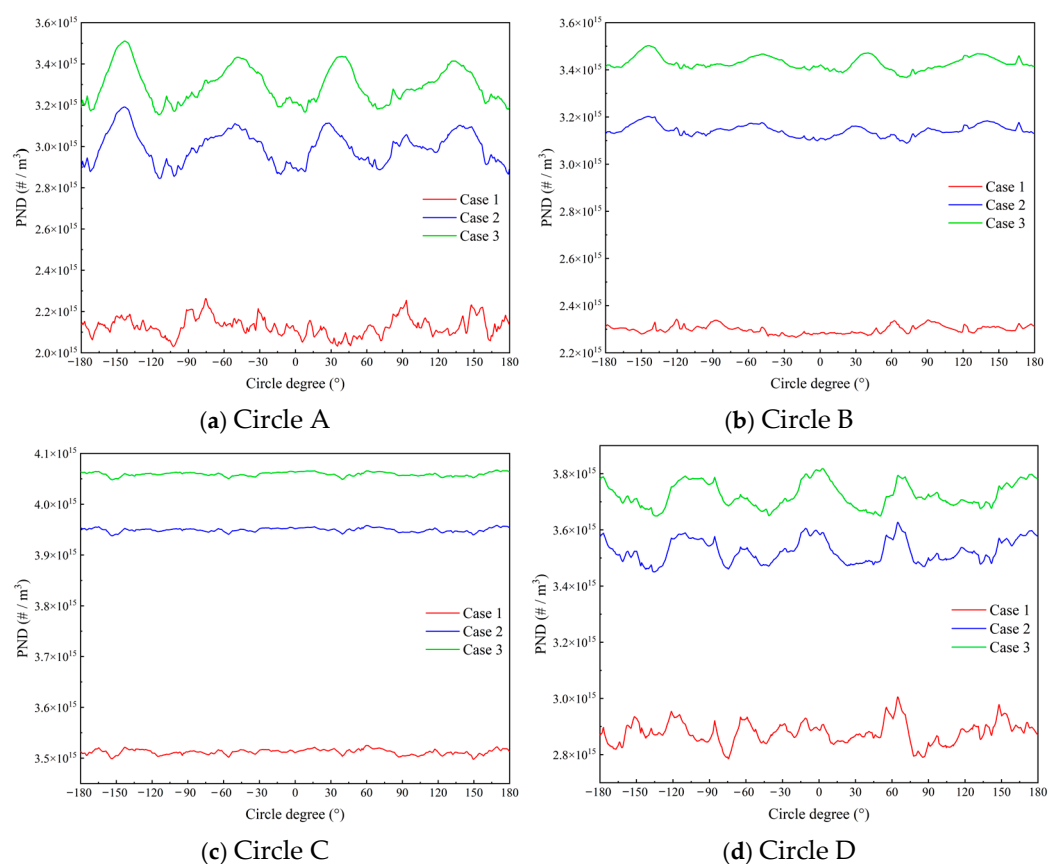


Figure 7. PND on circles A, B, C, and D.

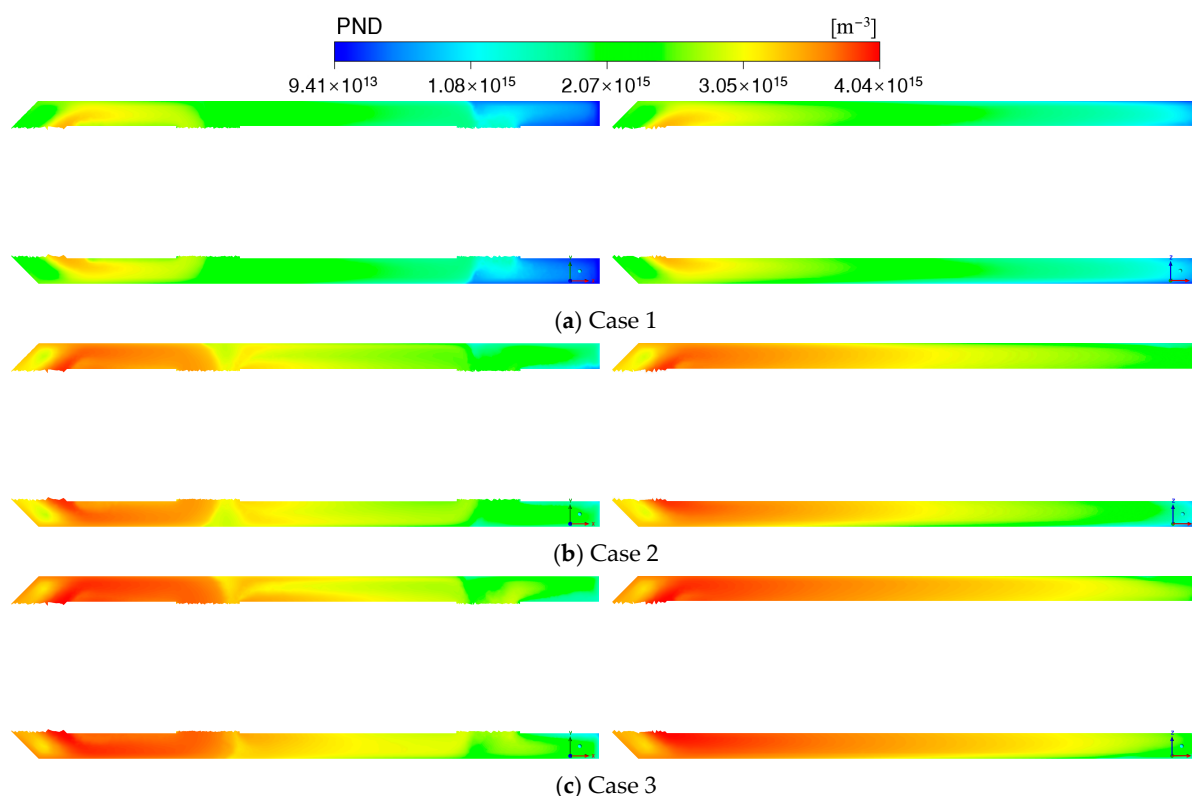
Table 3. The average pressure gradient between circles B, C, D, and circle A.

	Case 1	Case 2	Case 3
Pressure gradient between circle B-A (Pa/m)	122	1603	4293
Pressure gradient between circle C-A (Pa/m)	2540	20,633	52,558
Pressure gradient between circle D-A (Pa/m)	1193	10,810	27,519

3.3. Particle Coagulation in Annular Chamber

Particles carried by the airflow enter the annular chamber from the conical chamber. The coagulation behavior of the particle flow within the annular chamber directly affects the motion and coagulation of particles in the airflow rushing area of the inner chamber.

Figure 8 presents the axial PND distribution on the cross-sections XY and XZ of three cases. PND on cross-sections XY and XZ is higher before the particles enter the first pair of rushing holes along the axial direction of the annular chamber. Near the first pair of rushing holes, a portion of the particles are entrained into the inner chamber, resulting in a significant decrease in PND. In the vicinity of the second pair of rushing holes, the remaining particles are entrained into the inner chamber along with coagulation, leading to a continued decrease in PND. The cross-section XZ is far from the rushing holes, and particles on this cross-section are only affected by coagulation and diffusion. Therefore, the PND decreases more slowly along the axial direction of the annular chamber in cross-section XZ.

**Figure 8.** PND on cross-sections XY (left) and XZ (right).

Three concentric circles with different radii on three radial annular cross-sections were selected. The three radial annular cross-sections are located at the chamber inlet side ($x_1 = 0.17475$ m), the center of the first pair of rushing holes ($x_1 = 0.222$ m), and the center of the second set of rushing holes ($x_2 = 0.376$ m). The three radii of the circles on the cross-sections are $R_1 = 0.04625$ m (referred to as the circle R_1), $R_0 = 0.0425$ m (referred to

as the circle R_0), and $R_2 = 0.03875$ m (referred to as the circle R_2), representing the outer, middle, and inner circles of the annular chamber, respectively. Figure 9 shows the positions of the annular cross-section and concentric circles.

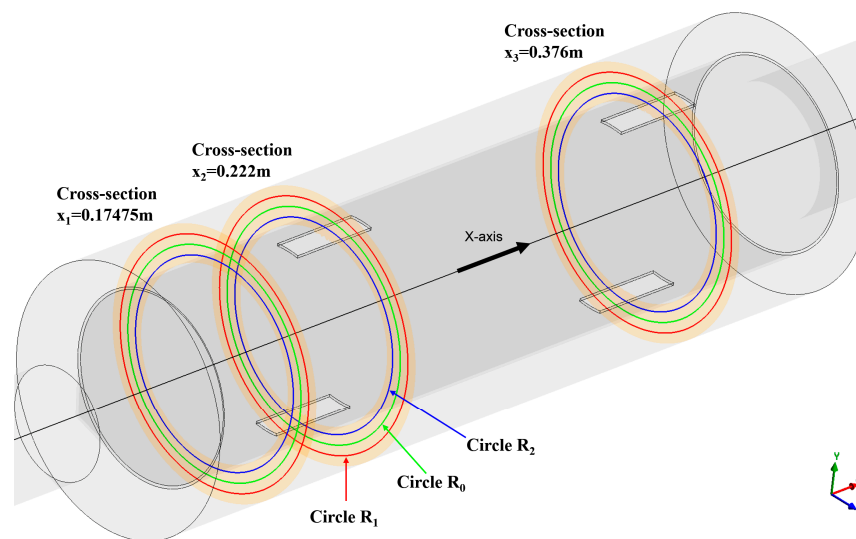


Figure 9. Sketch of annular cross-sections and concentric circles.

Table 4 presents the average airflow velocity and TKE on three concentric circles for three cases. Figure 10 presents the PND distribution on concentric circles and annular cross-section $x_1 = 0.17475$ m for three cases.

Table 4. Average airflow velocity and TKE on concentric circles of cross-section $x_1 = 0.17475$ m.

	Circle R_1		Circle R_0		Circle R_2	
	Velocity (m/s)	TKE (m^2/s^2)	Velocity (m/s)	TKE (m^2/s^2)	Velocity (m/s)	TKE (m^2/s^2)
Case 1	4.09	1.12	4.33	0.96	3.31	0.84
Case 2	12.09	8.19	12.90	6.48	9.95	5.20
Case 3	20.39	21.10	21.36	16.70	16.18	13.34

The intensification of turbulent eddies within the fluid due to high turbulent kinetic energy leads to increased relative velocities between particles caused by small-scale turbulent shear and random motion. Theoretically, these collisions promote particle coagulation, resulting in larger particles and a decrease in PND. However, while turbulent kinetic energy enhances spatial contact opportunities between particles, the ultimate coagulation effect is also influenced by particle residence time. High flow velocity results in shorter contact and interaction times, which may inhibit coagulation. As shown in Table 3 and Figure 10, on circle R_1 where the airflow collides with the outer chamber wall, the highest turbulent kinetic energy and relative velocity between particles coincide with a relatively high airflow velocity. Circle R_0 is in the middle of the annular chamber, the turbulent kinetic energy is moderate, and the airflow velocity is highest. With circle R_2 being near the inner chamber wall, both turbulent kinetic energy and airflow velocity are lowest. In regions with high turbulent kinetic energy and high flow velocity, these two factors may have a “competitive” effect on particle coagulation. The lowest PND on circle R_1 indicates that the effect of turbulent kinetic energy dominates.

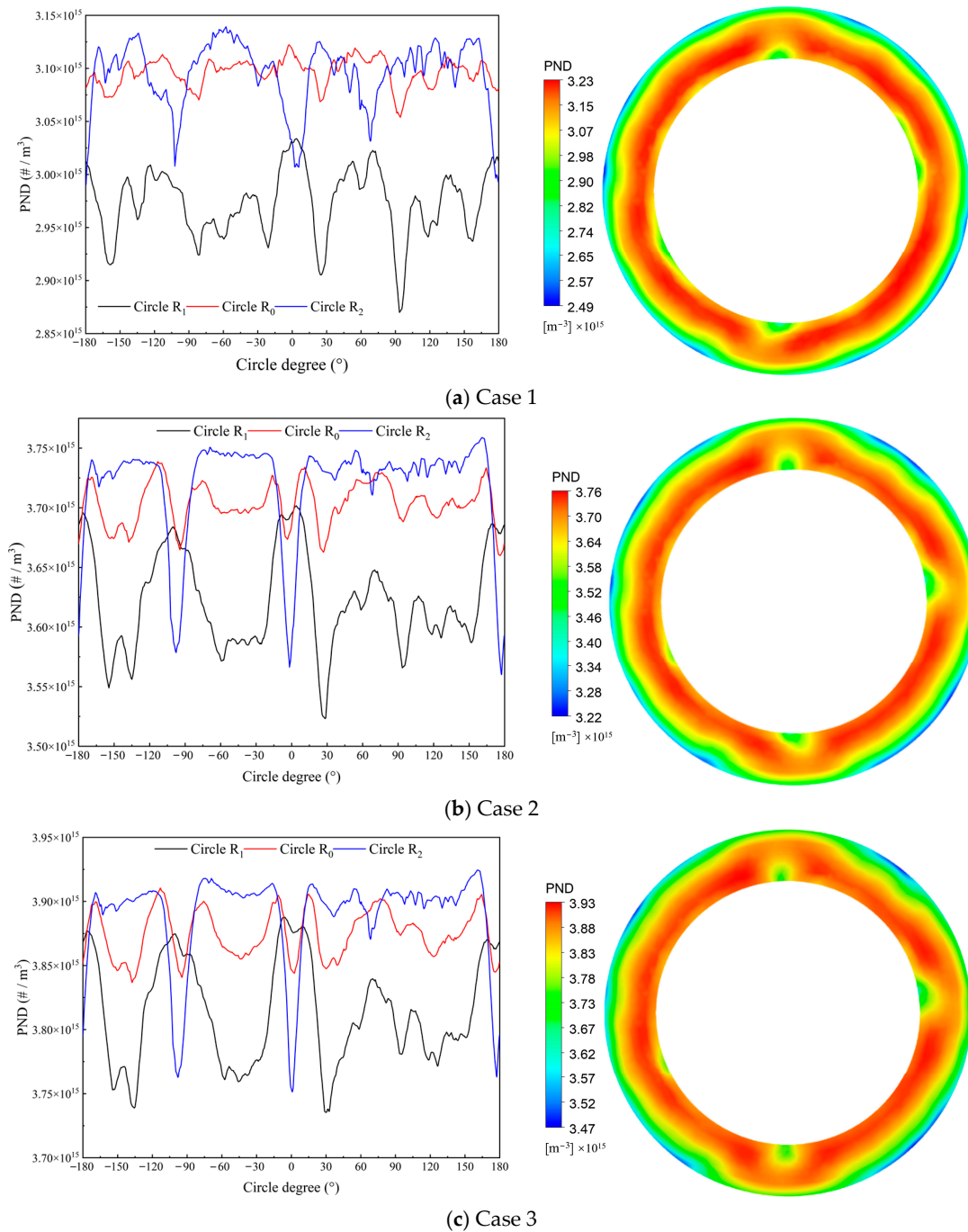


Figure 10. PND on concentric circles (left) and annular cross-section $x_1 = 0.17475$ m (right).

Figure 11 shows the velocity and turbulent kinetic energy distributions on three concentric circles on the cross-section $x_2 = 0.222$ m for three cases. For case 1 with an inlet velocity of 10 m/s, the peak velocity on the circle R_2 reaches 6.9 m/s. This can be attributed to the lower flow rate in case 1, which leads to a larger reverse flow zone above the first pair of rushing holes, as depicted in Figure 12. The interaction between the reverse flow and the incoming flow at circle R_1 and circle R_0 causes a substantial reduction in velocity, with the most pronounced effect observed at circle R_1 . Consequently, the velocity at the rushing hole location on circle R_1 is the lowest. The combined effects of collision and mixing on the flow at circle R_0 result in a higher velocity valley compared to that on circle R_1 . The flow on the circle R_2 is primarily composed of the main flow of the annular chamber and a portion of the mixed flow resulting from the collision. The high velocity and turbulent kinetic energy

of these two components contribute to the highest velocity and turbulent kinetic energy at the 0° and $\pm 180^\circ$ positions on circle R_2 . The figure further reveals that the velocity and turbulent kinetic energy at other circle positions exhibit low values and relatively stable behavior. This can be explained by the reduced influence of the reverse flow zone as the distance from the rushing hole increases, the velocity distribution is uniform and low at the $\pm 90^\circ$ positions.

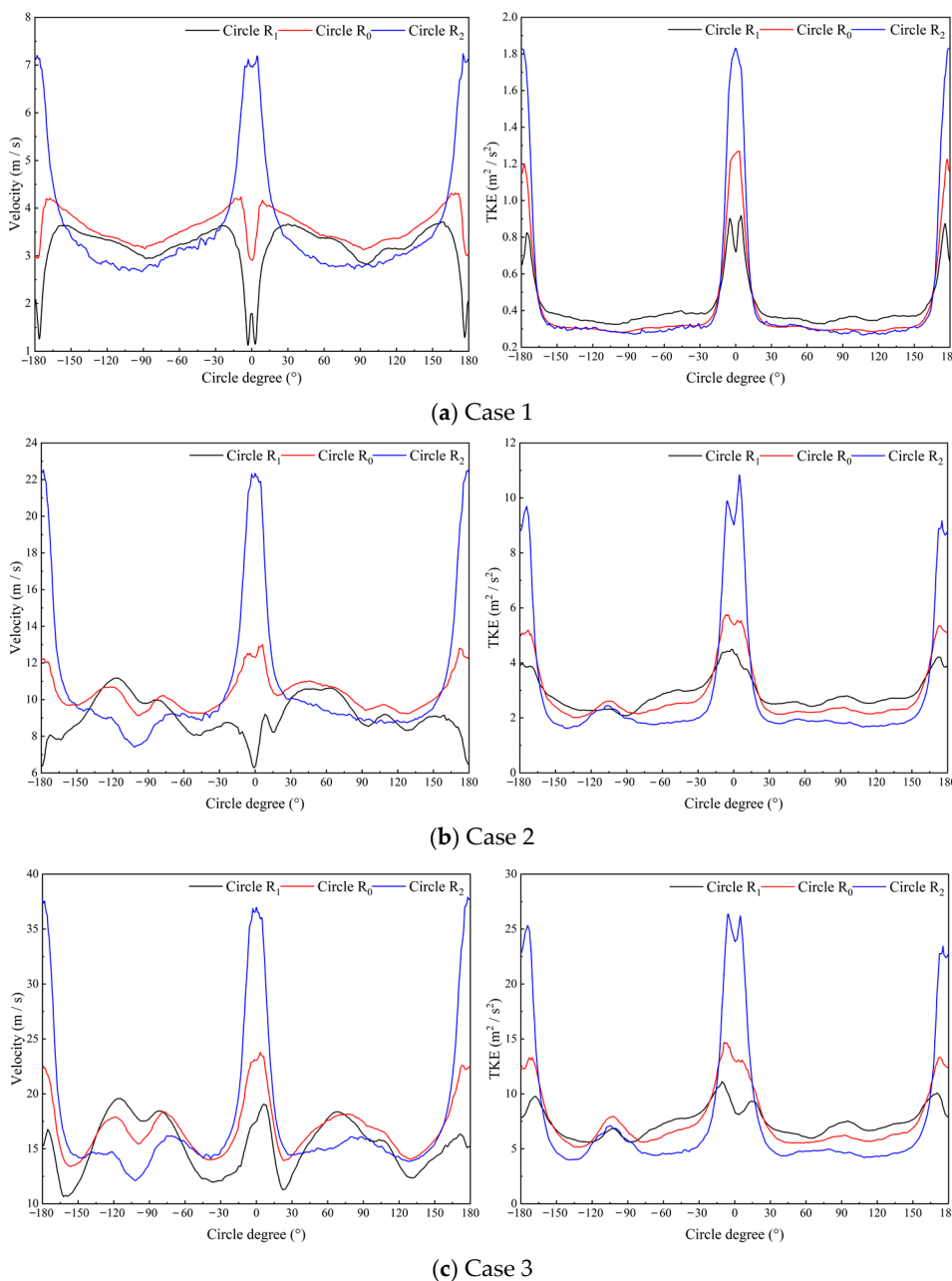


Figure 11. Velocity (left) and TKE (right) on three concentric circles on the cross-section $x_2 = 0.222$ m.

The velocity distributions on circle R_2 for cases 2 and 3 exhibit similar trends to case 1, with peaks occurring at 0° and $\pm 180^\circ$ and increasing with the inlet velocity. However, the velocity distributions on circle R_0 and circle R_1 undergo changes. For case 2, the velocity valleys at 0° and $\pm 180^\circ$ on circle R_1 increase to 6.3 m/s, while a peak of 12.5 m/s appears on circle R_0 . This is attributed to the reduced reverse flow zone at the rushing holes due to the increased flow rate, as shown in Figure 12b. The diminished reverse flow zone implies weaker collision between the main flow and the reverse flow, allowing more main flow to

enter the region and thus increasing the velocity valley. On circle R_0 , the flow is entirely dominated by the main flow. In case 3, the velocity peaks on all three circles continue to rise, with the peak on circle R_0 reaching 23.3 m/s and that on circle R_2 reaching 36.9 m/s. The velocity distribution on circle R_1 experiences the most significant change, with a peak of 18.4 m/s appearing at the rushing hole. This is due to the further reduction in the reverse flow zone on circle R_1 , as illustrated by the velocity vectors in Figure 12c. At this point, the reverse flow zone characteristic of low flow rate conditions is almost entirely occupied by the main flow, and the flow field is dominated by the main flow, leading to increased velocities. It is worth noting that increasing the flow rate reduces the influence of the reverse flow zone, but due to the persistent and intensified entrainment effect of the rushing holes with increasing flow rate, it is necessary to reduce the impact of flow reversal in all cases by increasing the width or optimizing the shape of the rushing holes.

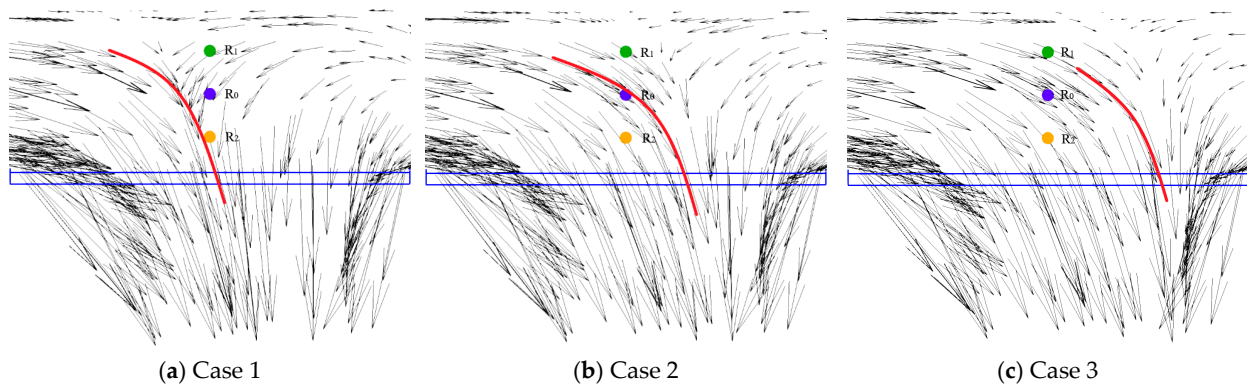


Figure 12. Sketch of reverse flow zone above the first pair of rushing holes.

Figure 13 presents the PND distributions on concentric circles and annular cross-section $x_2 = 0.222$ m for three cases. In case 1, the PND on the circle R_1 is the lowest among the three positions. This can be attributed to the lowest velocity and highest turbulent kinetic energy on the circle R_1 under this case. The enhanced turbulent kinetic energy typically indicates the presence of significant velocity gradients and complex flow structures, which promote inter-particle collisions. On the other hand, it also intensifies particle dispersion. Particle collisions and coagulation, coupled with dispersion-induced dilution, contribute to the decrease in PND. Meanwhile, the reduced velocity allows finer particles more residence time in the fluid, increasing the opportunities for turbulence-induced collisions and coagulation. Notably, the PND valleys at 0° and $\pm 180^\circ$ on the circle R_1 are the lowest, suggesting the most effective particle coagulation at these locations. This is due to the presence of recirculation vortices at 0° and $\pm 180^\circ$ on the circle R_1 , which intensify particle dispersion and coagulation.

Figure 14 presents the velocity and turbulent kinetic energy distributions on three concentric circles on the cross-section $x_3 = 0.376$ m for three cases. Compared with cross-section $x_2 = 0.222$ m, velocity peaks appear on the circle R_2 at 0° and $\pm 180^\circ$ positions for cross-section $x_3 = 0.376$ m, while small velocity valleys appear on the circle R_0 and circle R_1 . However, the overall trend is consistent with that of circle R_2 . This is because there is also a reverse flow zone above the second pair of rushing holes, and the range of the reverse flow zone is wider than that of the first pair of rushing holes, as shown in Figure 15. Since the circles are located within the reverse flow zone, the velocity peaks on circles R_1 , R_0 , and R_2 are caused by recirculation. Reverse flow also intensifies the velocity fluctuations of the fluid, forming certain velocity gradients and pressure gradients, which promote fluid mixing. Therefore, the turbulent kinetic energy also peaks at this location. The velocity reaches a minimum at the $\pm 90^\circ$ positions, as the influence of the

reverse flow zone decreases with increasing distance from the rushing hole on the circle. From the velocity vector plots in Figure 15, it can be seen that the reverse flow zone of case 3 is slightly shifted to the left, while the extent and shape of the reverse flow zone for other cases do not change significantly with increasing velocity. Therefore, the velocity and turbulent kinetic energy distributions are similar.

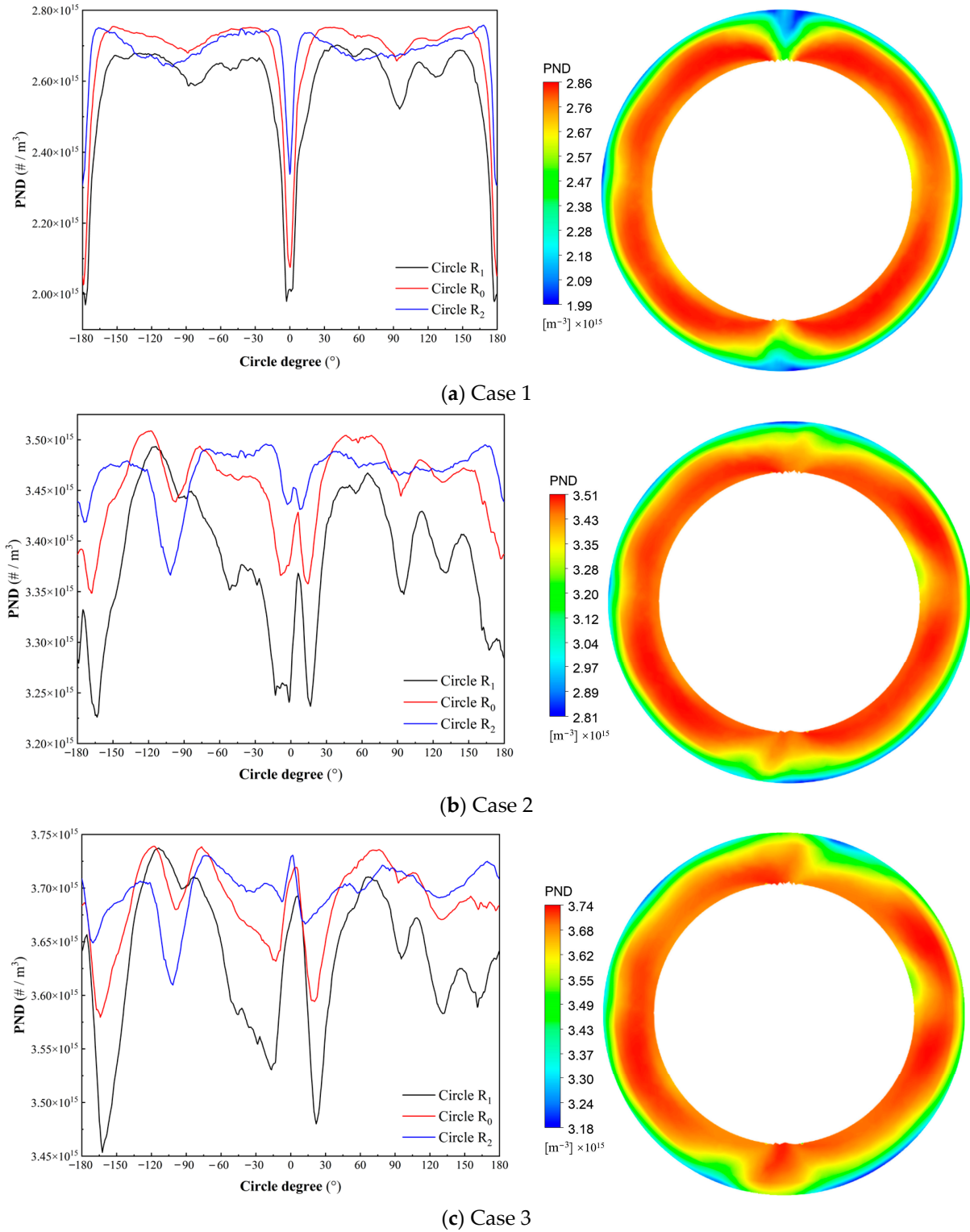


Figure 13. PND on concentric circles (left) and annular cross-section $x_2 = 0.222$ m (right).

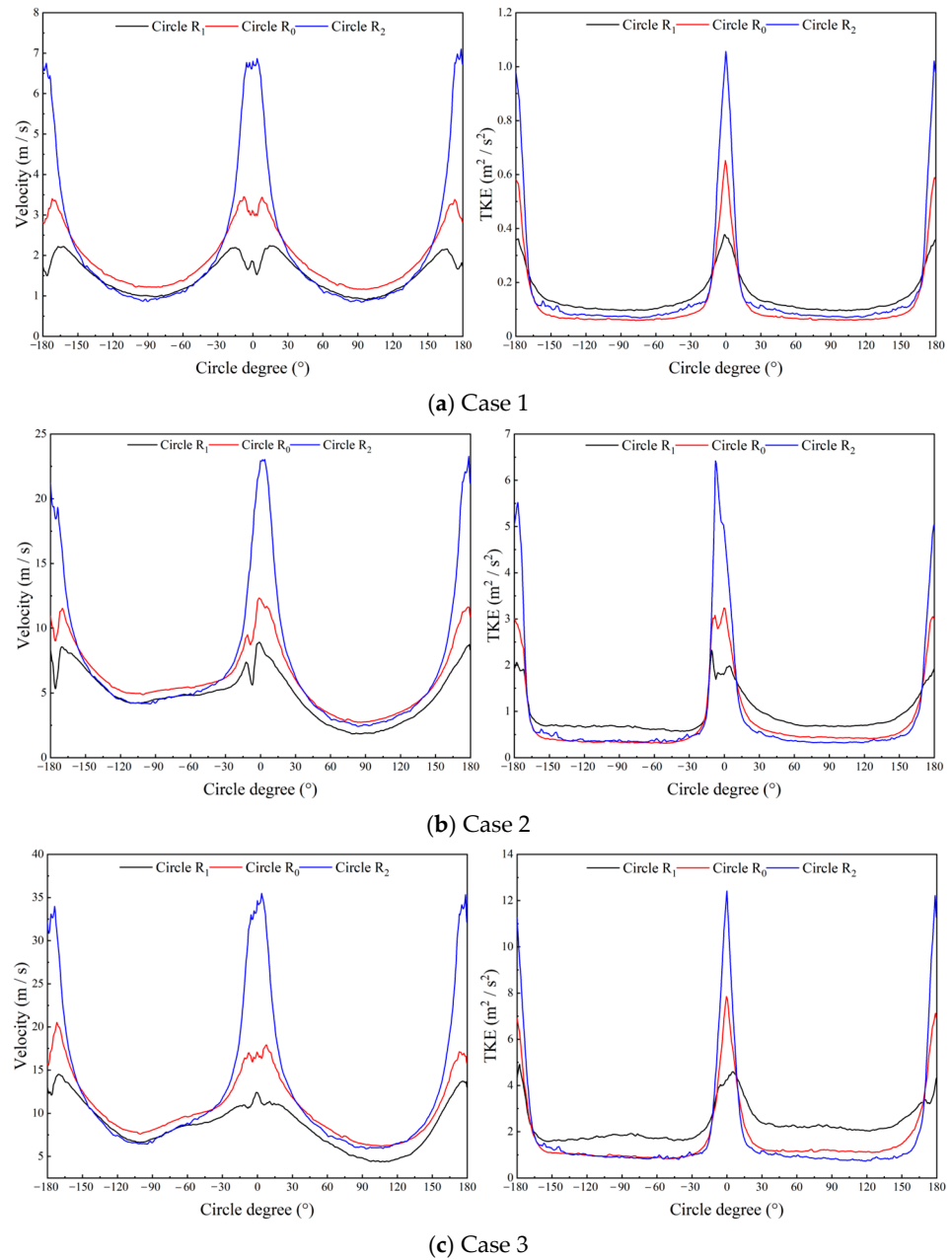


Figure 14. Velocity (left) and TKE (right) on three concentric circular cross-section $x_3 = 0.376$ m.

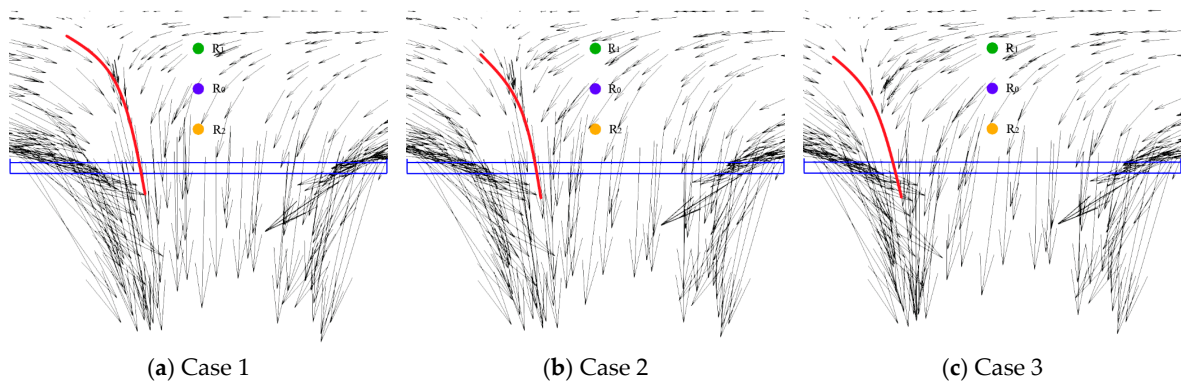


Figure 15. Sketch of reverse flow zone above the second pair of rushing holes.

Figure 16 presents the PND distributions on concentric circles and annular cross-section $x_3 = 0.376$ m for three cases. The formation of PND valleys at 0° and $\pm 180^\circ$ positions is attributed to reverse flow and vortices, similar to that on the cross-section $x_2 = 0.222$ m. It can be observed that the PND on the cross-section $x_3 = 0.376$ m is smaller than that on the cross-section $x_2 = 0.222$ m for three cases due to the coagulation effect. Moreover, the PND exhibits smaller fluctuations at positions other than 0° and $\pm 180^\circ$, indicating a higher degree of uniformity compared to the cross-section $x_2 = 0.222$ m.

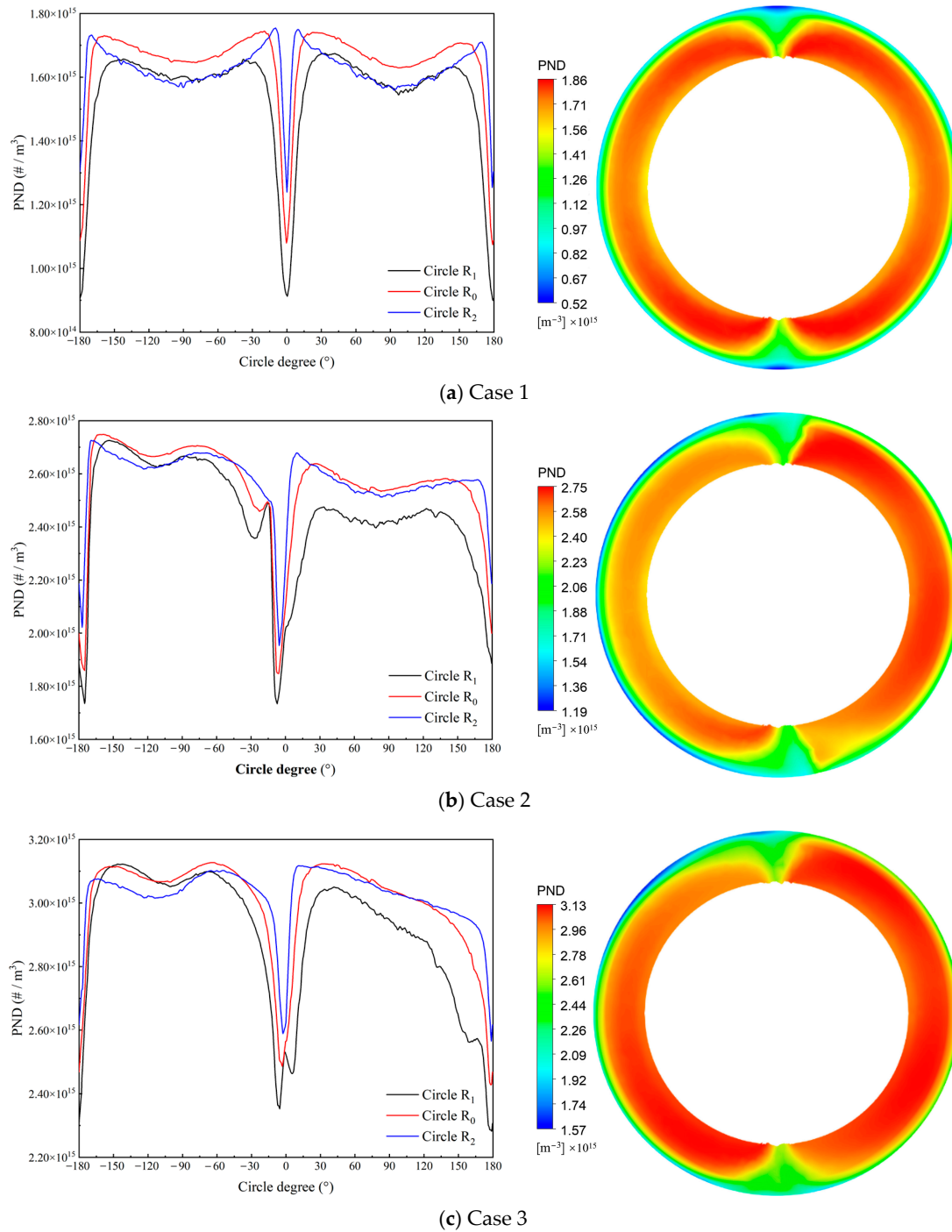


Figure 16. PND on concentric circles (left) and annular cross-section $x_3 = 0.376$ m (right).

3.4. Particle Coagulation in Inner Chamber

The inner chamber serves as the most concentrated zone for nanoparticle collision and coagulation, playing a pivotal role in the overall coagulation process.

Figure 17 presents the velocity and PND on the cross-sections XY and XZ in the inner chamber. The airflow enters the inner chamber from the annular chamber through the rushing holes at a certain angle, accelerating at the rushing holes and increasing its kinetic energy. Table 5 shows the flow velocity at two pairs of rushing holes.

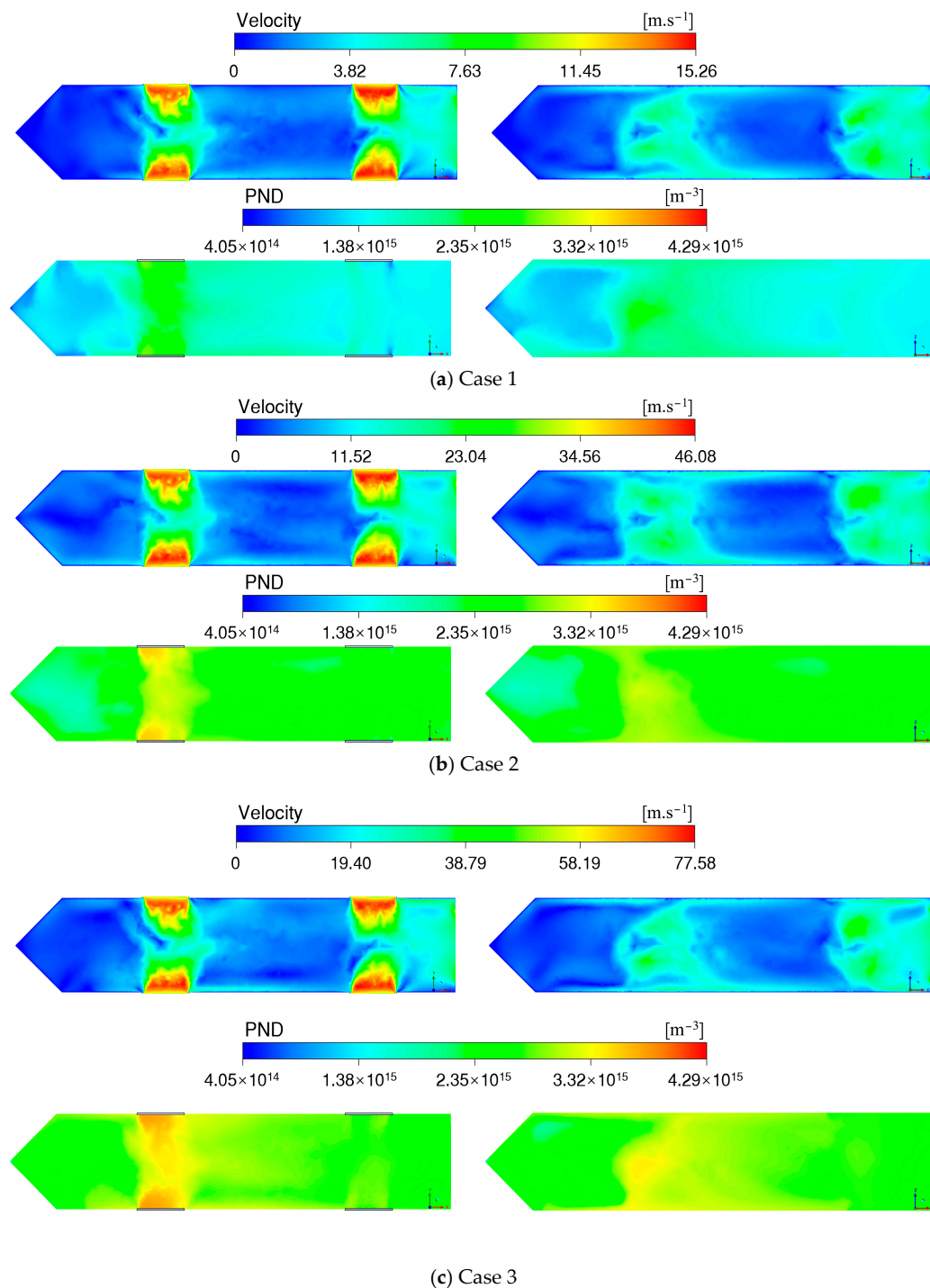


Figure 17. Velocity and PND on XY and XZ cross-section (**top left:** velocity of cross-sections XY; **top right:** velocity of cross-sections XZ; **bottom left:** TKE of cross-sections XY; **bottom right:** TKE of cross-sections XZ).

Table 5. Airflow velocity and its amplification at the rushing holes.

	First Pair of Rushing Holes		Second Pair of Rushing Holes	
	Velocity (m/s)	Amplification (%)	Velocity (m/s)	Amplification (%)
Case 1	14.5	45.0	15.0	50.0
Case 2	44.0	46.7	45.4	51.3
Case 3	73.7	47.4	75.7	51.4

The accelerated airflow collides near the axial centerline, generating intense turbulence. This turbulence induces random motion of nanoparticles within the airflow, thereby increasing the collision frequency among particles. As shown in Figures 12 and 15, two streams of airflow enter the inner chamber from the rushing holes at a certain angle, with their velocity components in the X-direction pointing towards the positive X-direction. The resultant velocity vectors, obtained by vector addition of their individual velocity components, also point towards the positive X-direction, indicating that the airflow moves in the positive X-direction. Only a small portion of the airflow moves in the negative X-direction after collision. Therefore, a small amount of low-velocity particulate flow exists in the space between the guiding cone surface and the first pair of rushing holes, resulting in a lower PND in this region.

The coagulation characteristics of particles were investigated on three radial cross-sections ($x'_1 = 0.1475$ m, $x'_2 = 0.222$ m, $x'_3 = 0.376$ m) within the inner chamber, which were perpendicular to the X-axis and aligned with the annular chamber cross-sections, as shown in Figure 18. Additionally, radial positions in the Y and Z directions on the cross-sections x'_2 and x'_3 were examined.

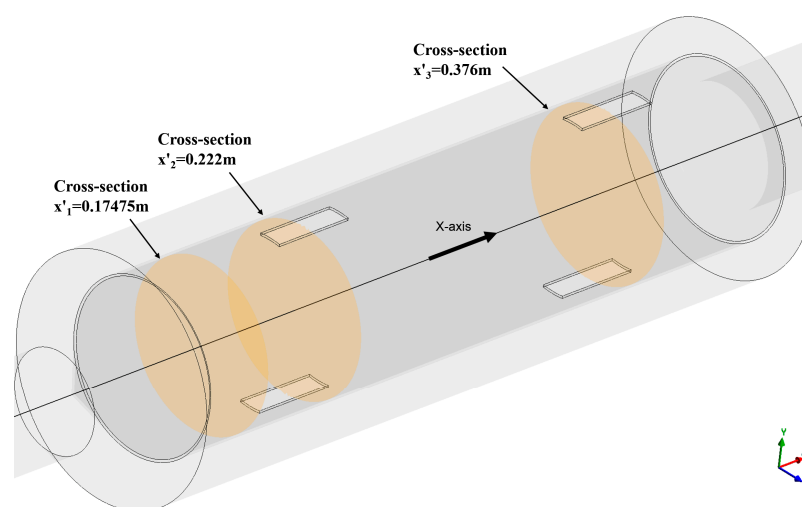
**Figure 18.** Sketch of three radial cross-sections in the inner chamber.

Figure 19 presents the PND and particle diameter distributions on the cross-section $x'_1 = 0.1475$ m for three cases. As analyzed in the previous section, the particulate flow involved in the rushing primarily moves in the positive X-direction, while the flow in the negative X-direction is relatively small. Coupled with the coagulation of particles, the PND at the $x'_1 = 0.1475$ m cross-section is relatively low, and the particle size is larger.

Figure 20 illustrates that the Z-directional airflow, upon colliding with the inner chamber wall, induces a bent flow field with a significant pressure gradient. The bent airflow, in conjunction with the Y-directional airflow, gives rise to four vortex regions. As the airflow moves inward from the vortex periphery, the decreasing radius necessitates a reduced velocity at the center of the vortex region to conserve angular momentum. The figure further demonstrates that in case 3, while the airflow at the rushing holes exhibits

greater disturbance, the vortex structure remains intact. The vortex region initiated by the first pair of rushing holes extends to the middle of the inner chamber, whereas the vortex region initiated by the second pair of rushing holes persists until the inner chamber outlet.

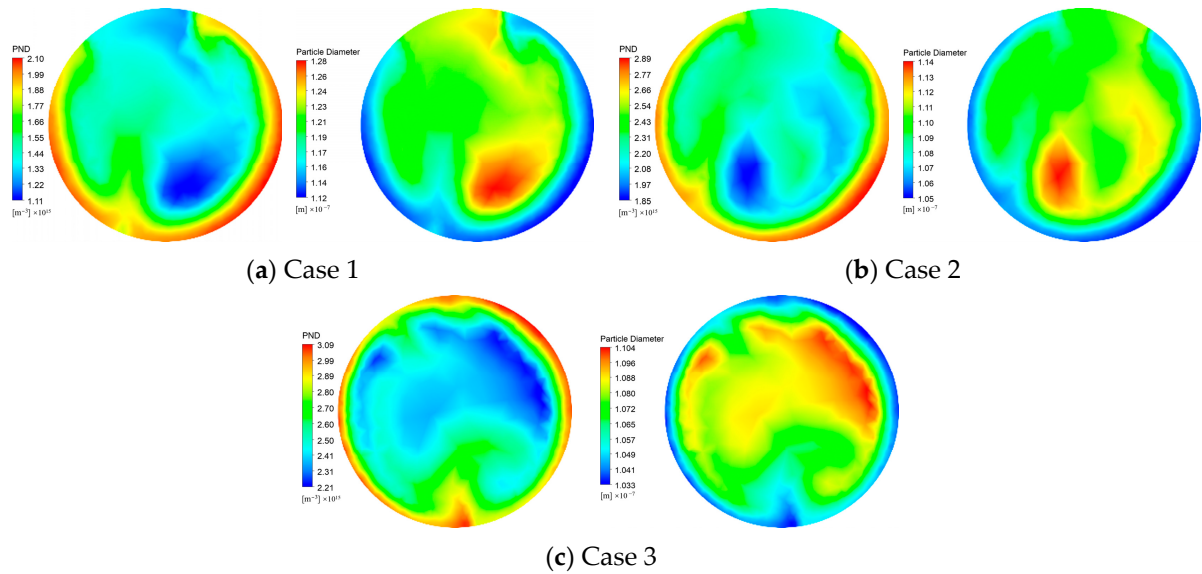


Figure 19. PND (left) and particle diameter (right) on cross-section $x'_1 = 0.1475$ m.

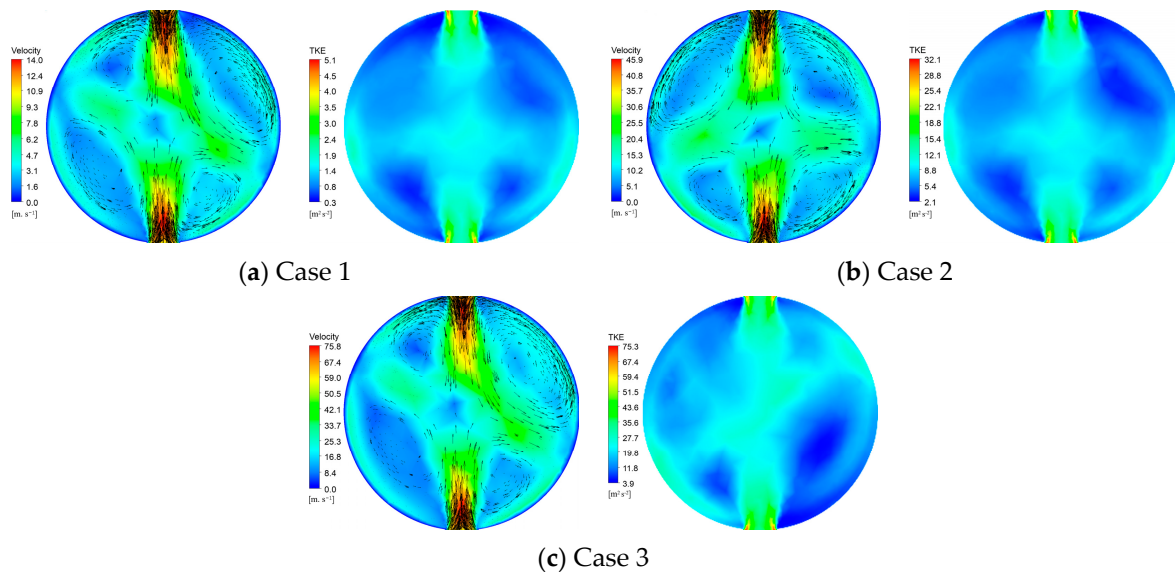


Figure 20. Velocity (left) and TKE (right) on cross-section $x'_2 = 0.222$ m.

Figures 21 and 22 present the radial PND distributions at the rushing holes on the cross-section $x'_2 = 0.222$ m and $x'_3 = 0.376$ m for three cases, respectively. The radial PND distributions of the two sets of rushing holes exhibit differences. The PND in the Y-radial direction increases initially as the airflow carrying a large amount of particles enters the inner chamber from the first pair of rushing holes. The PND then decreases due to the enhanced coagulation as the airflow continues to move towards the rushing center, reaching a minimum near the center. For the Z-radial direction, a peak in PND appears near the rushing center due to the short-term influx of a large number of particles. The PND then decreases towards the wall due to coagulation and increases slightly near the wall due to the influence of particles from the outer region of the vortices. The PND of the second pair of rushing holes is lower than that of the first pair due to coagulation. The radial

PND distribution is not radially symmetric, especially for case 2 and case 3, which exhibit asymmetric distributions. This is attributed to the highly irregular and non-uniform nature of turbulence, which increases with flow velocity. Especially in regions with local flow non-uniformities or rapid changes in velocity gradients, the turbulence characteristics on both sides of the radial direction cannot be identical. The PND distributions of the second pair of rushing holes in both the Y and Z directions are similar but exhibit higher asymmetry. This is because the second pair of rushing holes is not only affected by the reverse flow from above the rushing holes, as discussed above, but also by the axial inflow. The superposition of these two flows within the second pair of rushing holes leads to a more non-uniform PND distribution.

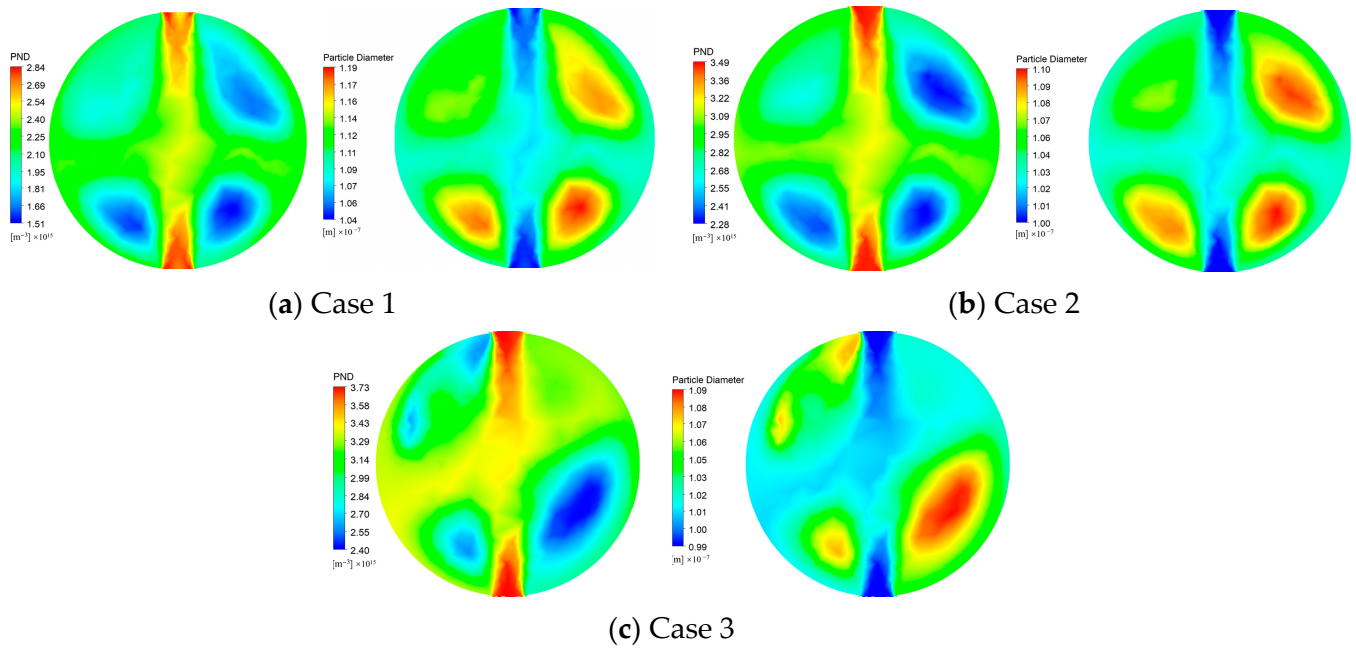


Figure 21. PND (left) and particle diameter (right) on cross-section $x'_2 = 0.222$ m.

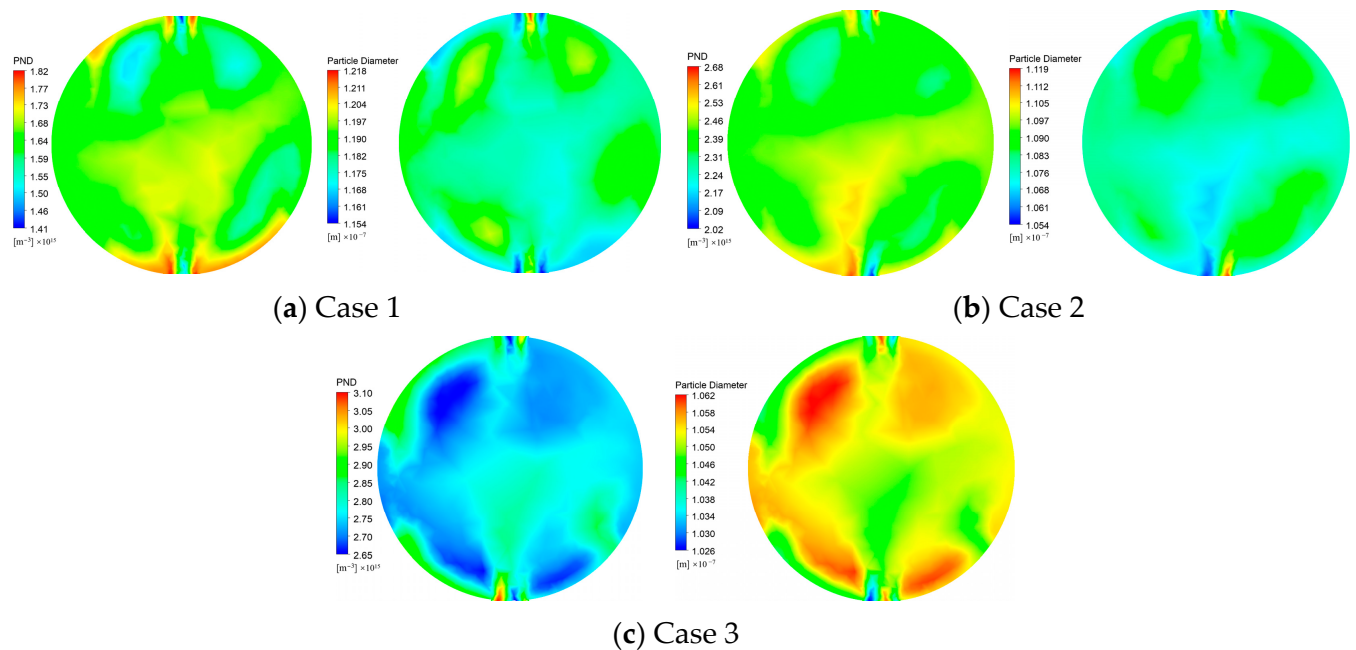


Figure 22. PND (left) and particle diameter (right) on cross-section $x'_4 = 0.376$ m.

The uniformity index is a metric used to quantify the spatial variation in a specified field variable within a defined region or on a given surface. The uniformity index can be weighed by either area or mass. The area-weighted uniformity index, also known as the Gamma uniformity index, reflects the distribution of quantity and is defined as the ratio of the mean value of variable φ over the area $\bar{\varphi}$ to its standard deviation, as expressed by the following equation:

$$\gamma = 1 - \frac{1}{2} \cdot \frac{\sum_{i=1}^n [(|\varphi_i - \bar{\varphi}|) A_i]}{|\bar{\varphi}| \cdot \sum_i^n A_i} \quad (19)$$

where A_i denotes the area of the element mesh. When variable φ represents the flow velocity, the above equation expresses the flow uniformity index γ_{flow} . When variable φ represents the number density of particles, the above equation expresses the particle number density uniformity index γ_{PND} .

Table 6 presents the velocity and PND uniformity indices on the radial circle cross-section of the inner chamber for three cases. A large amount of airflow enters the chamber through the first pair of rushing holes at $x'_2 = 0.222$ m. As analyzed above, the high-speed airflow is mainly distributed in the Y and Z radial directions, while the four vortex regions contain low-speed airflow, leading to the largest variation in velocity distribution on this cross-section. Therefore, the velocity uniformity index on this cross-section is the lowest. With the increase in flow rate, the diffusion of airflow is enhanced, and the PND uniformity index on this cross-section increases. The velocity uniformity indices on other cross-sections are all above 0.8, and the PND uniformity indices are all above 0.93. A uniform airflow velocity means that all particles have an equal chance to collide and coagulate with other particles, and it reduces the locally high particle concentration, thus increasing the PND uniformity index. A higher particle number density uniformity index under various cases or operating conditions also implies that the device can maintain higher stability and sustain good performance even under fluctuating load conditions.

Table 6. Velocity and PND uniformity index on the radial circle cross-sections.

	$x'_1 = 0.1475$ m		$x'_2 = 0.222$ m		$x'_3 = 0.376$ m	
	γ_{flow}	γ_{PND}	γ_{flow}	γ_{PND}	γ_{flow}	γ_{PND}
Case 1	0.838	0.930	0.763	0.933	0.820	0.986
Case 2	0.835	0.957	0.774	0.957	0.819	0.987
Case 3	0.803	0.965	0.767	0.956	0.828	0.992

3.5. Particle Coagulation Efficiency

The evolution of particle diameter distribution at the outlet pipe over time can be used to evaluate the final coagulation effect. Taking case 2 as an example, Figure 23 shows the particle diameter distribution as a function of PND at the end of the outlet tube at different times. The results show that as time increases, small particles coagulate to form larger particles, and the total number of particles in the system decreases. The coagulation process causes the particles to shift towards larger diameters. In the initial stage of coagulation, the PND decreases rapidly. As time progresses, the particle diameter increases, the collision efficiency of particles decreases, and the coagulation rate slows down. During this stage, the particle diameter growth rate slows down, and the width of the particle diameter distribution increases, leading to enhanced dispersity.

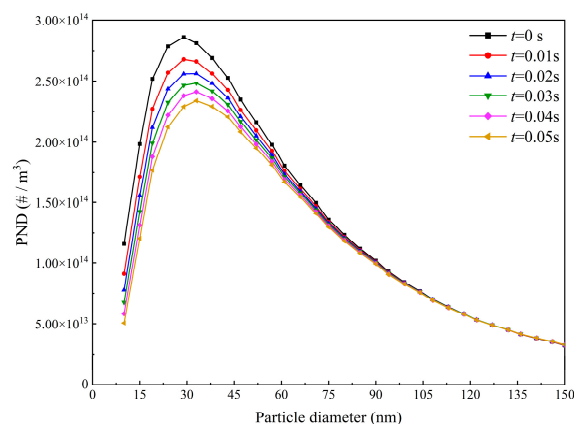


Figure 23. Distribution of particle diameter with PND at different simulation times at outlet of case 2.

Figure 24 illustrates the PND at the device outlet at 10.0 s for three cases. It can be observed that for low-speed cases, the peak of PND shifts towards larger particle diameters, indicating a higher degree of particle diameter dispersion and better coagulation efficiency. In contrast, for high-speed cases, the peak particle diameter shifts to a lesser extent, and the peak value of PND is higher.

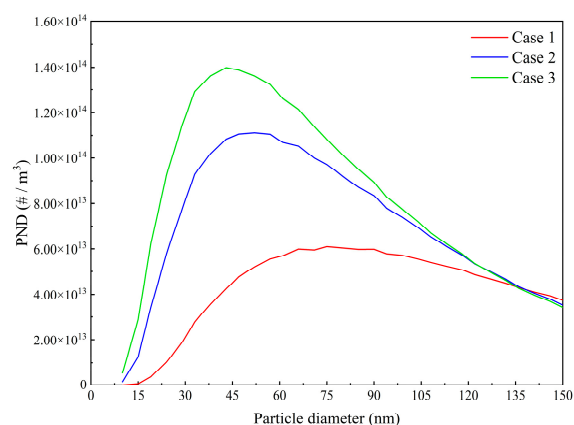


Figure 24. Distribution of particle diameter at the outlet with PND of three cases.

The coagulation process led to an increase in the average particle diameter from 96 nm to 121 nm for case 1, while for case 2 and case 3, the average particle diameter increased to 110 nm and 107 nm, respectively.

The overall particle coagulation efficiency (η_{all}), the nucleation mode particle coagulation efficiency (η_{nucl}), and the accumulation mode particle coagulation efficiency (η_{accu}) are given by the following equations:

$$\eta_{all} = \frac{N_{all_in} - N_{all_out}}{N_{all_in}} \times 100\% \quad (20)$$

$$\eta_{nucl} = \frac{N_{nucl_in} - N_{nucl_out}}{N_{nucl_in}} \times 100\% \quad (21)$$

$$\eta_{accu} = \frac{N_{accu_in} - N_{accu_out}}{N_{accu_in}} \times 100\% \quad (22)$$

The coagulation efficiencies for three cases are shown in Table 7. Case 1 exhibited the highest overall coagulation efficiency of 59.73%, while the coagulation efficiency was lower for high flow velocity conditions, primarily due to the combined effects of particle residence time and temperature. Under high-velocity exhaust flow conditions, although the

exhaust temperature is also high, the reduction in particle residence time plays a dominant role in decreasing the coagulation efficiency; thus, the impact of particle residence time predominates.

Table 7. Particle coagulation efficiency for three cases.

	Case 1	Case 2	Case 3
η_{all} (%)	59.73	33.91	22.21
η_{nucl} (%)	88.89	64.57	49.75
η_{accu} (%)	29.95	2.55	−5.96

The coagulation efficiency of nucleation-mode particles was higher than that of accumulation-mode particles, which is mainly attributed to the physical properties and coagulation mechanisms of nucleation-mode particles. For diesel engine exhaust, the number of nucleation-mode particles far exceeds that of accumulation-mode particles, leading to a higher number density of nucleation-mode particles per unit volume. Brownian motion facilitates frequent collisions between these particles, resulting in increased coagulation. From the perspective of particle dynamics, nucleation-mode particles have a larger surface-area-to-volume ratio, making them more susceptible to interactions and coagulation with other particles. In contrast, accumulation-mode particles, due to their larger diameter and smaller surface-area-to-volume ratio, have a lower initial number density per unit volume, resulting in a lower probability of collisions and thus lower coagulation efficiency. It is noteworthy that the coagulation efficiency of accumulation-mode particles in case 3 is less than zero, indicating that a large number of nucleation-mode particles coagulate to form larger accumulation-mode particles during the coagulation process, leading to a shift in the particle diameter distribution towards larger sizes.

The symmetric arrangement of the two pairs of rectangular rushing holes along the central axis enables the scalability of the device, allowing it to function effectively across various engine sizes without altering the fundamental mechanism of particle impingement and coagulation. However, the differences in exhaust gas properties, such as temperature, velocity, and pressure, between engines with varying displacement and power can impact the coagulation efficiency. Future work will focus on conducting bench tests with different types of diesel engines to evaluate the device's performance under diverse operating conditions and further validate its scalability.

4. Conclusions

This study investigated the effects of flow field characteristics on the evolution of diesel engine exhaust particulate matter number concentration and the coagulation efficiency of fine particles in a newly designed diesel engine exhaust split-stream rushing coagulation device. Through theoretical analysis and numerical simulation, the flow field characteristics, nanoparticle motion characteristics, and coagulation characteristics of the split-stream rushing device were studied. The main conclusions are as follows:

- (1) An annular vortex ring is induced near the guiding cone surface. The PND at the center of the vortex ring is lower than that in the outer region of the vortex ring and the main flow region for all cases. Due to the combined influence of the main flow and the outer edge of the vortex ring, the PND at the transition position is between that of the main flow region and the outer region of the vortex ring. The PND in the main flow region is the highest.
- (2) The PND in the annular chamber is relatively high before the particles enter the first pair of rushing holes. The airflow near the rushing holes is simultaneously influenced by the airflow from the conical chamber and the entrainment effect of the rushing

holes, resulting in the formation of vortices in the latter half of the two sets of rushing holes; however, the airflow away from the rushing holes is only affected by the airflow from the conical chamber and flowed stably in the X-direction.

- (3) The velocity uniformity index exhibits the lowest value at the cross-section of $x'_2 = 0.222$ m. As the flow rate increases, the diffusion of airflow is enhanced, leading to an increase in the PND uniformity index on the cross-section of $x'_2 = 0.222$ m. The velocity uniformity indices on other cross-sections exceed 0.8, and the PND uniformity indices surpass 0.93.
- (4) The overall coagulation efficiency of case 1 is the highest, reaching 59.73%, while those of case 2 and case 3 are 33.91% and 22.21%, respectively. The coagulation of particles caused the average outlet particle diameter of case 1 to increase from 96 nm to 121 nm, and those of case 2 and case 3 increased to 110 nm and 107 nm, respectively. The coagulation efficiency of nucleation-mode particles is higher than that of accumulation-mode particles.

Author Contributions: Conceptualization, Y.G. and P.W.; methodology, Y.G.; software, Y.G. and P.H.; validation, Y.G. and P.W.; formal analysis, Y.G.; investigation, Y.G.; resources, P.W. and H.S.; data curation, Y.G., J.X. and Y.Z.; writing—original draft preparation, Y.G.; writing—review and editing, Y.G. and P.W.; visualization, Y.G.; supervision, P.W.; project administration, P.W.; funding acquisition, P.W. and H.S. All authors have read and agreed to the published version of the manuscript.

Funding: This research was funded by the Natural Science Foundation of Inner Mongolia Autonomous Region, grant number 2023MS05022; Basic Research Fund for Institutions of Inner Mongolia Autonomous Region, grant number BR230155; and Natural Science Foundation of Inner Mongolia Autonomous Region, grant number 2024MS05039.

Data Availability Statement: The original contributions presented in the study are included in the article.

Conflicts of Interest: The authors declare no conflicts of interest.

Abbreviations

PM-particulate matter; IJM/IJR-impinging jet mixers/reactors; PIV-particle image velocimetry; CFD-computational fluid dynamics; LES-large eddy simulation; RANS-Reynolds-Averaged Navier–Stokes; RNG-re-normalization group; PBE-population balance equation; NDF-number density function; UDF-user defined functions; TKE-turbulent kinetic energy; PND-particle number density.

References

1. Oravisjärvi, K.; Pietikäinen, M.; Ruuskanen, J.; Niemi, S.; Laurén, M.; Voutilainen, A.; Keiski, R.L.; Rautio, A. Diesel particle composition after exhaust after-treatment of an off-road diesel engine and modeling of deposition into the human lung. *J. Aerosol Sci.* **2014**, *69*, 32–47. [[CrossRef](#)]
2. Kittelson, D.B.; Watts, W.F.; Johnson, J.P.; Rowntree, C.J.; Goodier, S.P.; Payne, M.J.; Preston, W.H.; Warrens, C.P.; Ortiz, M.; Zink, U.; et al. *Driving Down On-Highway Particulate Emissions*; SAE International: Warrendale, PA, USA, 2006. [[CrossRef](#)]
3. Sharma, N.; Mitra, K.; Pezer, J.; Pathak, R.; Sjöblom, J. Characterization from Diesel and Renewable Fuel Engine Exhaust: Particulate Size/Mass Distributions and Optical Properties. *Aerosol Sci. Eng.* **2023**, *7*, 182–191. [[CrossRef](#)]
4. Chen, S.; Chang, S.; Chen, Y.; Chen, H. Possible warming effect of fine particulate matter in the atmosphere. *Commun. Earth Environ.* **2021**, *2*, 208. [[CrossRef](#)]
5. Flood-Garibay, J.A.; Angulo-Molina, A.; Méndez-Rojas, M.Á. Particulate matter and ultrafine particles in urban air pollution and their effect on the nervous system. *Environ. Sci. Process. Impacts.* **2023**, *4*, 704–726. [[CrossRef](#)]
6. Environmental Protection Agency. Control of Emissions of Air Pollution from Nonroad Diesel Engines and Fuel. *Notes* **2004**, *69*, 4213.
7. EPA. Emission Standards for Nonroad Engines and Vehicles. Available online: <https://www.epa.gov/emission-standards-reference-guide/epa-emission-standards-nonroad-engines-and-vehicles> (accessed on 23 August 2024).

8. Dallmann, T.; Shao, Z.; Menon, A.; Bandivadekar, A. Non-Road Engine Technology Pathways and Emissions Projections for the Indian Agricultural and Construction Sectors. In *SAE Technical Paper*; SAE International: Warrendale, PA, USA, 2017. [[CrossRef](#)]
9. Shen, X.; Kong, L.; Shi, Y.; Cao, X.; Li, X.; Wu, B.; Zhang, H.; Yao, Z. Multi-type Air Pollutant Emission Inventory of Non-road Mobile Sources in China for the Period 1990–2017. *Aerosol Air Qual. Res.* **2021**, *21*, 210003. [[CrossRef](#)]
10. Landgrebe, J.D.; Pratsinis, S.E. A discrete-sectional model for particulate production by gas-phase chemical reaction and aerosol coagulation in the free-molecular regime. *J. Colloid. Interface Sci.* **1990**, *139*, 63–86. [[CrossRef](#)]
11. Ji, J.H.; Hwang, J.; Bae, G.N.; Kim, Y.G. Particle charging and agglomeration in DC and AC electric fields. *J. Electrostat.* **2004**, *61*, 57–68. [[CrossRef](#)]
12. Kilikevičienė, K.; Kačianauskas, R.; Kilikevičius, A.; Maknickas, A.; Matijošius, J.; Rimkus, A.; Vainorius, D. Experimental investigation of acoustic agglomeration of diesel engine exhaust particles using new created acoustic chamber. *Powder Technol.* **2020**, *360*, 421–429. [[CrossRef](#)]
13. Jia, Y.; Yang, Z.; Bu, S.; Xu, W. Experimental investigation on the agglomeration performance of pre-charged micro-nano particles in uniform magnetic field. *Chem. Eng. Res. Des.* **2024**, *201*, 523–533. [[CrossRef](#)]
14. Zhou, L.; Yang, S.Y.; Chen, W.; Wang, X.B.; Yuan, Z.L.; Yang, L.J.; Wu, H. Chemical agglomeration properties of fine particles immersed in solutions and the reduction in fine particle emission by adding emulsion polymers. *Fuel Process. Technol.* **2018**, *175*, 44–53. [[CrossRef](#)]
15. Barbosa, F.V.; Teixeira, S.F.; Teixeira, J.C. Convection from multiple air jet impingement—A review. *Appl. Therm. Eng.* **2023**, *218*, 119307. [[CrossRef](#)]
16. Uddin, N.; Weigand, B.; Younis, B.A.; Lyulinetsky, R.; Ali, K. Flow and heat transfer dynamics of an altered impinging plane jet using an insert. *Int. Commun. Heat. Mass. Transf.* **2024**, *150*, 107151. [[CrossRef](#)]
17. Zhang, J.; Liu, M.; Dong, X.; Feng, Y. Study on the Turbulent Vortex Structure Characteristics of a Two-Layer Impinging Stream Reactor. *Chem. Eng. Technol.* **2024**, *2*, 268–274. [[CrossRef](#)]
18. Liu, X.; Yue, S.; Lu, L.; Gao, W. Experimental and Numerical Studies on Flow and Turbulence Characteristics of Impinging Stream Reactors with Dynamic Inlet Velocity Variation. *Energies* **2018**, *7*, 1717. [[CrossRef](#)]
19. Pal, S.; Madane, K.; Mane, M.; Kulkarni, A.A. Impingement Dynamics of Jets in a Confined Impinging Jet Reactor. *Ind. Eng. Chem. Res.* **2021**, *2*, 969–979. [[CrossRef](#)]
20. Lindstedt, R.P.; Luff, D.S.; Whitelaw, J.H. Velocity and Strain-Rate Characteristics of Opposed Isothermal Flows. *Flow. Turbul. Combust.* **2005**, *2*, 169–194. [[CrossRef](#)]
21. Hao, Y.; Seo, J.H.; Hu, Y.; Mao, H.Q.; Mittal, R. Flow physics and mixing quality in a confined impinging jet mixer. *AIP Adv.* **2020**, *10*, 045105. [[CrossRef](#)] [[PubMed](#)]
22. Zhang, J.W.; Ding, C.W.; Dong, X.; Feng, Y.; Ma, F.R. Experimental study on the flow field characteristics of the two-layer impinging stream mixer. *Can. J. Chem. Eng.* **2021**, *12*, 2748–2759. [[CrossRef](#)]
23. Bie, H.; Xue, L.; Wang, Y.; Liu, G.; Hao, Z.; An, W. Flow regimes and mixing performance in T-T jet reactor. *Chem. Eng. Process. Process Intensif.* **2022**, *170*, 108700. [[CrossRef](#)]
24. Yin, Z.Q.; Lin, J.Z. Numerical simulation of the formation of nanoparticles in an impinging twin-jet. *J. Hydrodyn.* **2007**, *19*, 533–541. [[CrossRef](#)]
25. Liu, X.D.; Chen, Y.P.; Chen, Y.F. Analysis of gas-particle flow characteristics in impinging streams. *Chem. Eng. Process. Process Intensif.* **2014**, *79*, 14–22. [[CrossRef](#)]
26. Hubbard, J.A.; Cheng, M.D.; Cheung, L.; Kirsch, J.R.; Richards, J.M.; Fugate, G.A. UO₂F₂ particulate formation in an impinging jet gas reactor. *React. Chem. Eng.* **2021**, *8*, 1428–1447. [[CrossRef](#)]
27. Li, Q.Y.; Wang, X.Z. Population balance and CFD simulation of particle aggregation and growth in a continuous confined jet mixer for hydrothermal synthesis of nanocrystals. *Crystals* **2021**, *2*, 144. [[CrossRef](#)]
28. Launder, B.E.; Spalding, D.B. The Numerical Computation of Turbulent Flows. *Comput. Methods Appl. Mech. Eng.* **1974**, *2*, 269–289. [[CrossRef](#)]
29. Gelbard, F.; Tambour, Y.; Seinfeld, J.H. Sectional representations for simulating aerosol dynamics. *J. Colloid. Interface Sci.* **1980**, *2*, 541–556. [[CrossRef](#)]
30. Matsoukas, T.; Friedlander, S.K. Dynamics of aerosol agglomerate formation. *J. Colloid. Interface Sci.* **1991**, *146*, 495–506. [[CrossRef](#)]
31. Pletcher, R.H.; Tannehill, J.C.; Anderson, D. *Computational Fluid Mechanics and Heat Transfer*; CRC Press: Warrendale, PA, USA, 2012.
32. Lee, K.W.; Liu, B.Y.H. Theoretical study of aerosol filtration by fibrous filters. *Aerosol Sci. Technol.* **1982**, *1*, 147–161. [[CrossRef](#)]
33. Allen, M.D.; Raabe, O.G. Slip correction measurements of spherical solid aerosol particles in an improved Millikan apparatus. *Aerosol Sci. Technol.* **1985**, *4*, 269–286. [[CrossRef](#)]
34. Otto, E.; Fissan, H. Brownian coagulation of submicron particles. *Adv. Powder Technol.* **1999**, *10*, 1–20. [[CrossRef](#)]
35. Otto, E.; Fissan, H.; Park, S.H.; Lee, K.W. The log-normal size distribution theory of Brownian aerosol coagulation for the entire particle size range: Part II—Analytical solution using Dahneke’s coagulation kernel. *J. Aerosol Sci.* **1999**, *30*, 17–34. [[CrossRef](#)]

36. Pratsinis, S.E.; Kim, K.S. Particle coagulation, diffusion and thermophoresis in laminar tube flows. *J. Aerosol Sci.* **1989**, *20*, 101–111. [[CrossRef](#)]
37. Saffman, P.G.F.; Turner, J.S. On the collision of drops in turbulent clouds. *J. Fluid. Mech.* **1956**, *1*, 16–30. [[CrossRef](#)]
38. Zaichik, L.I.; Solov'Ev, A.L. Collision and coagulation nuclei under conditions of Brownian and turbulent motion of aerosol particles. *High. Temp.* **2002**, *40*, 422–427. [[CrossRef](#)]
39. Tan, P.Q.; Ruan, S.S.; Hu, Z.Y.; Lou, D.M.; Li, H. Particle number emissions from a light-duty diesel engine with biodiesel fuels under transient-state operating conditions. *Appl. Energy* **2014**, *113*, 22–31. [[CrossRef](#)]
40. Xue, J.; Li, Y.; Wang, X.; Durbin, T.D.; Johnson, K.C.; Karavalakis, G.; Asa-Awuku, A.; Villela, M.; Quiros, M.; Hu, S.; et al. Comparison of vehicle exhaust particle size distributions measured by SMPS and EEPS during steady-state conditions. *Aerosol Sci. Technol.* **2015**, *49*, 984–996. [[CrossRef](#)]
41. Kuuluvainen, H.; Karjalainen, P.; Saukko, E.; Ovaska, T.; Sirviö, K.; Honkanen, M.; Olin, M.; Niemi, S.; Keskinen, J.; Rönkkö, T. Nonvolatile ultrafine particles observed to form trimodal size distributions in non-road diesel engine exhaust. *Aerosol Sci. Technol.* **2020**, *54*, 1345–1358. [[CrossRef](#)]

Disclaimer/Publisher's Note: The statements, opinions and data contained in all publications are solely those of the individual author(s) and contributor(s) and not of MDPI and/or the editor(s). MDPI and/or the editor(s) disclaim responsibility for any injury to people or property resulting from any ideas, methods, instructions or products referred to in the content.